Feasibility and Performance Analysis of Neptune Aerocapture Using Heritage Blunt-Body Aeroshells

Athul Pradeepkumar Girija,* Sarag J. Saikia,† and James M. Longuski‡
Purdue University, West Lafayette, Indiana 47907
and
Shyam Bhaskaran,§ Matthew S. Smith,¶ and James A. Cutts**
California Institute of Technology, Pasadena, California 91109

Large navigation and atmospheric uncertainties have historically driven the need for a mid-lift-to-drag-ratio (mid-L/D) vehicle with $(L/D)_{max}$ of 0.6–0.8 for aerocapture at Neptune. Most planetary entry vehicles flown to date are low-L/D blunt-body aeroshells with L/D less than 0.4. The lack of a heritage mid-L/D aeroshell presents a major hurdle for Neptune aerocapture, as the development of a new entry vehicle incurs significant time and investment. Techniques that may allow Neptune aerocapture to be feasible using heritage low-L/D blunt-body aeroshells are investigated that obviate the need for mid-L/D aeroshells. A navigation study is performed to quantify the delivery errors, and a new guidance algorithm with onboard density estimation is developed to accommodate large atmospheric uncertainties. Monte Carlo simulation results indicate that the reduced navigation uncertainty and improved guidance scheme enable a blunt-body aeroshell with $L/D = 0.3$–0.4 to perform aerocapture at Neptune. The expected heat rate is within the capabilities of existing thermal protection system materials.

I. Introduction

AEROCAPTURE is a maneuver in which a spacecraft uses aerodynamic drag to decelerate and perform orbit insertion. Neptune's great heliocentric distance and the need to achieve reasonable flight time lead to high arrival V_∞ and large orbit insertion ΔV. Propulsive insertion incurs significant mass penalty due to the large ΔV, where aerocapture is a promising alternative. Aerocapture at Neptune has been shown to substantially increase delivered mass and allow reduction in flight time compared with propulsive insertion [1–3]. Despite the potential benefits, aerocapture at Neptune presents significant challenges related to vehicle design and thermal protection system (TPS) materials. The large navigation and atmospheric uncertainties drive the need for a vehicle with sufficient control authority to perform aerocapture without the spacecraft risking escape or undershooting the target capture orbit [4].

Several mission concepts and technology demonstration flights have proposed the use of aerocapture, but it has never been flown [5–9]. Hall et al. [10] showed that aerocapture could enhance missions to Venus, Mars, Titan, and Uranus and enable some missions to Jupiter, Saturn, and Neptune. Heritage low-lift-to-drag-ratio ($L/D \leq 0.4$) blunt-body aeroshells and existing TPS materials are sufficient for aerocapture at Venus, Mars, and Titan [4,11–14]. Aerocapture studies have historically used a mid-lift-to-drag-ratio (mid-L/D) vehicle with L/D of 0.6–0.8 to accommodate the large navigation and atmospheric uncertainties at Uranus and Neptune [15–19]. Aerocapture at Jupiter and Saturn is considered a long-term goal due to the extreme aerothermal conditions during the atmospheric pass [4].

Until the early 2000s most aerocapture studies address feasibility at Earth and Mars, though some generic aerocapture studies evaluate its applicability at Uranus and Neptune [20,21]. Detailed study of aerocapture at Neptune began only in the early 2000s due to a multicenter NASA effort funded by the In-Space Technology Program [11,22–28]. The study concluded that aerocapture at Neptune is feasible using a vehicle with L/D of 0.6–0.8 and can deliver 1.4 times more mass to orbit compared with propulsive orbit insertion. In 2016, Spilker et al. [4] performed a study initiated by the NASA Planetary Science Division to assess the readiness of aerocapture at all planetary destinations. The study concluded that aerocapture at Uranus and Neptune call for at least an additional study to assess the need for mid-L/D vehicles that require significant development and testing before use on planetary missions. The study recommends quantifying delivery errors at Neptune, investigation of improved flight control techniques, and other mission concepts such as pathfinder probes that may reduce the vehicle L/D requirement.

In 2016, Saikia et al. [19] performed an assessment of aerocapture at Uranus and Neptune in support of the NASA Ice Giants Pre-Decadal Survey Mission Study [29]. Saikia et al. demonstrated the importance of coupling between interplanetary arrival conditions and aerocapture feasibility at Uranus and Neptune. The study concluded that mid-L/D vehicles (L/D of 0.6–0.8) are required at Uranus and Neptune to accommodate the uncertainties, using uncertainty estimates available from Lockwood et al. [1]. Development and testing of a new mid-L/D vehicle requires substantial funding commitment and at least a decade's time. This merits investigation of approaches that obviate the need for mid-L/D vehicles. The study recommended several directions of future work:

1) Studies should investigate the feasibility of high-energy fast arrival interplanetary trajectories that allow for more control authority compared with conventional trajectories used for propulsive insertion architectures.

2) Studies need to be performed to better quantify the relevant uncertainties such as delivery errors from approach navigation and atmospheric uncertainties.

3) Approaches such as guidance schemes with onboard density estimation, hybrid aerocapture-propulsive techniques, and a pathfinder entry probe should be investigated.

One or a combination of these techniques may allow the use of a heritage low-L/D vehicle for Neptune aerocapture, thus obviating the need for a new mid-L/D vehicle, and leads to the objectives of the present study:

1) The first objective of this study is to assess the feasibility of Neptune aerocapture using heritage blunt-body aeroshells with L/D of 0.4 or less.

2) The second objective is to provide statistical metrics of aerocapture vehicle performance using a representative interplanetary trajectory incorporating the state-of-the-art knowledge in navigation, atmospheric, and aerodynamic uncertainties.

In 2019, the NASA Outer Planets Analysis Group reiterated the potential and benefits offered by aerocapture for ice giant missions [30]. When combined with aerocapture, the Space Launch System (SLS) would enable trip times to Uranus and Neptune to be as short as 5 and 7 years, respectively. Aerocapture offers substantial savings in flight time compared with a nominal 12 years to Uranus and more than 13 years to Neptune compared with propulsive insertion architectures. The Planetary Science Decadal Survey recommends a Uranus orbiter with probe as the third-highest priority Flagship-class mission in the next decade, after Mars Sample Return and Europa orbiter [31]. Between Uranus and Neptune, more difficult requirements of achieving orbit at Neptune appear to be the reason for Uranus being preferred over Neptune [31]. There is significant scientific interest in Neptune and Triton, as evident in the evaluation of mission concepts for both Uranus and Neptune in the NASA Ice Giants Pre-Decadal Mission Study [29] and the ESA Ice Giants Study [32]. Aerocapture strongly enhances and in some cases enables missions to either of the ice giants without being constrained by a substantial propulsive insertion mass penalty due to the large orbit insertion ΔV [2–4]. The present study aims to consolidate the state-of-the-art knowledge of aerocapture mission design to allow scientists, mission designers, and program managers to assess its readiness for a future ice giant mission.

II.   Aerocapture Trade Space and Feasibility Analysis

Previous Neptune aerocapture studies have often been restricted to analysis of a single-point design with limited exploration of the underlying trade space. Multiple aerocapture studies have used a limited number of candidate interplanetary trajectories and vehicle designs to perform aerocapture systems analysis, and quantify the performance benefits compared with propulsive insertion [1,10,11,13,33]. The interplanetary trajectories are often optimized for propulsive insertion, and do not take into account the often differing requirements for aerocapture. In addition to the mass benefit, aerocapture can allow significantly shorter time of flights for outer solar system missions compared with propulsive insertion. Hughes [34] has compiled a catalog of short-time-of-flight, high-arrival V_∞ trajectories to Uranus and Neptune, though their aerocapture feasibility aspects are yet to be investigated. Such high V_∞ trajectories greatly widen the interplanetary trajectory options for missions to Uranus and Neptune.

To accommodate for the large uncertainties at Uranus and Neptune the aerocapture vehicle must have sufficiently large L/D. All interplanetary entry missions flown to date have used ballistic or low-L/D vehicles ($L/D \leq 0.4$) and are considered high-heritage entry systems. Studies investigating aerocapture at Neptune have used a mid-L/D vehicle (L/D of 0.6–0.8), assuming that such a vehicle would be available. The nonavailability of a mid-L/D vehicle presents a major hurdle for aerocapture at the ice giant planets. The present study introduces an approach to determine the required vehicle L/D considering a broad set of interplanetary trajectories and vehicle designs. In addition to the previously mentioned issues for aerocapture systems, constraints arising from launch vehicle performance, entry deceleration loads, and aerodynamic heating are considered. The present work uses the "aerocapture feasibility chart" for rapid trade space exploration unifying interplanetary trajectory and vehicle design aspects of the problem.

Figure 1 shows the aerocapture feasibility chart for Neptune. The left-side chart shows the arrival V_∞, time of flight, and launch C_3 for a comprehensive set of interplanetary trajectories from Earth to Neptune and shows the tradeoff between these parameters for mission design. The trajectory data come from two sources: the NASA Ice Giants Pre-Decadal Mission Study [29], and a set of high V_∞ trajectories made available to the authors by the Jet Propulsion Laboratory. The trajectories include both relatively slow arrival (defined by $V_\infty \leq 15$ km/s) trajectories used for propulsive insertion and fast arrival ($15 < V_\infty \leq 25$ km/s) trajectories that are feasible only with orbit insertion using aerocapture. To perform aerocapture the vehicle must enter the atmosphere within a narrow range of entry flight-path angles (EFPAs) called the "theoretical corridor." Entering too steep results in the vehicle undershooting the target apoapsis and possibly encountering aerodynamic heating beyond the TPS limits. Entering too shallow results in the vehicle not getting captured. The right-side chart in Fig. 1 shows contours of the theoretical corridor width (TCW), peak deceleration, peak stagnation-point heat rate $\dot{q}$, and total heat load as a function of the arrival V_∞ and vehicle L/D. A nominal deceleration limit of $30g$ is imposed. For the peak heat rate constraint, 8000 W/cm^2 is used based on Heatshield for Extreme Entry Environment Technology (HEEET) test results [35], and a total heat load constraint of 600 kJ/cm^2 is used, which is about twice the nominal stagnation point heat load for the Galileo entry probe [36].

The green-shaded area shows the feasible combinations of $(L/D, V_\infty)$ for a TCW requirement of 2.0 deg [1], and deceleration and heating constraints bounding the feasible region. The bottom corner of the green-shaded region indicates the smallest L/D for which aerocapture is feasible if the required TCW = 2.0 deg. To minimize the required L/D, high arrival V_∞ trajectories are desired as
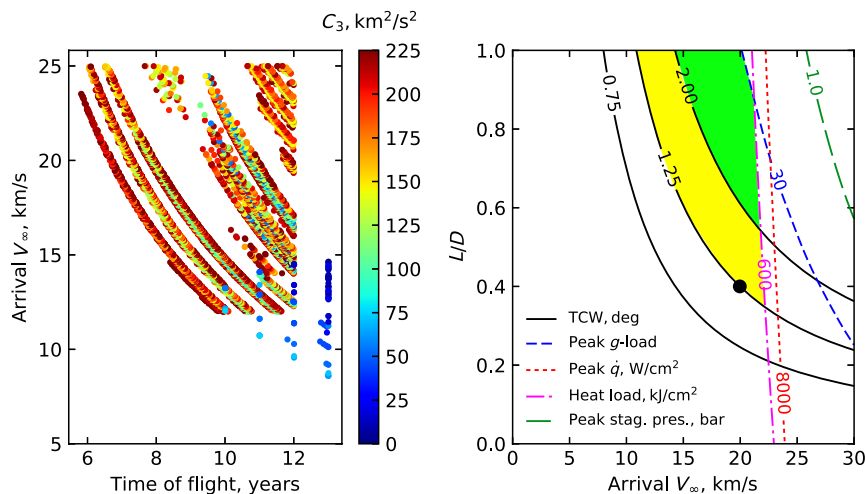

Fig. 1   Neptune aerocapture feasibility chart. The green region indicates the feasible design space for TCW requirement of 2.0 deg, for which the required L/D is 0.6–1.0 [1].

the higher entry speed allows a larger theoretical corridor compared with slow arrival trajectories. The fast arrival trajectories using aerocapture also allow significantly shorter time of flight to Neptune (<8 years) as compared with the conventional slow arrival trajectories using propulsive insertion ($\approx$13 years). Figure 1 shows that propulsive insertion and aerocapture require a different class of interplanetary trajectories. Propulsive insertion requires arrival V_∞ to be small enough such that the propulsion system can handle the capture burn. Short-time-of-flight trajectories typically have high arrival V_∞ and result in large propellant mass requirement, which in turn severely limits the useful delivered mass. On the other hand, aerocapture requires a high arrival V_∞ to minimize the L/D requirement. Interplanetary trajectories with arrival V_∞ less than a critical value (defined by vehicle L/D and the TCW requirement in Fig. 1) are infeasible for aerocapture. The range of feasible arrival V_∞ for aerocapture is bounded on the upper end by peak deceleration and TPS material and total heat load constraints.

The TCW requirement is computed based on the navigation, atmospheric, and aerodynamic uncertainties to be accommodated by the aerocapture vehicle, and it dictates the required L/D. The contributions of various uncertainties as quantified by Lockwood et al. [1] and the root-sum-squared required corridor width (RCW) are shown in Fig. 2. To ensure that the aerocapture vehicle achieves the desired atmospheric exit conditions, the TCW should be greater than the estimated RCW with adequate safety margin. Failure to satisfy this criterion implies the vehicle risks crashing into the planet or not getting captured. Based on the estimated RCW in Fig. 2, a TCW of at least 2.0 deg is required and the required L/D falls in the range of 0.6–1.0 as seen in Fig. 1. If the uncertainties are reduced (e.g., by reducing the delivery error) such that the TCW requirement is reduced to 1.25 deg, then the yellow-shaded region in Fig. 1 becomes feasible in addition to the green region. The reduced TCW requirement lowers the L/D requirement. Figure 1 shows that if the TCW requirement is lowered to 1.25 deg, fast arrival trajectories with $V_\infty \geq 20$ km/s allow the vehicle L/D requirement to be lowered to 0.4. The selected baseline design ($L/D = 0.4$, $V_\infty = 20$ km/s) is indicated by the black circle. Further reduction in L/D is possible if the uncertainties are reduced even further, and TCW requirement is reduced to 0.75 deg, which may allow a Mars Science Laboratory (MSL)–derived aeroshell with $L/D = 0.24$ to be used.

III. Aerocapture Mission Design

A reference interplanetary trajectory is selected to allow a future Cassini-style exploration of the Neptune system. A comprehensive set of trajectories considering a wide range of arrival V_∞ at Neptune is used to assess the broad interplanetary trajectory trade space. For the purpose of this study, a maximum allowable time of flight of 8 years is

considered (compared with the 13-year baseline used in the Ice Giants Pre-Decadal Study [29]). The minimum delivered mass requirement is 2000 kg to Neptune orbit, and SLS Block 1B is the baseline launch vehicle. Based on the allowable time of flight, delivered mass requirement at Neptune, and the available launch vehicle performance, a set of feasible candidate trajectories is considered. The study assumes the use of an Apollo-like blunt-body aerocapture vehicle with a total mass of approximately 5000 kg, with an additional 1000 kg allotment for a cruise stage jettisoned before the maneuver. The study assumes that 40% of the arrival mass (i.e., before aerocapture, which includes aeroshell structure, TPS, etc.) is delivered to orbit [10]. This results in about 2000 kg delivered to Neptune orbit, comparable to the dry mass of Cassini spacecraft at Saturn. Trajectories with C_3 low enough to satisfy the delivered mass requirement and also meet the flight time constraint are selected. For the feasible set of interplanetary trajectories the minimum required vehicle L/D can be computed from the right-side chart in Fig. 1 based on their arrival V_∞. If heritage blunt-body aeroshells are used, the L/D requirement must not exceed 0.4. The chart also demarcates constraints arising from deceleration loads, heat rate, and total heat load. Interplanetary trajectories that provide sufficient TCW and do not violate the peak deceleration, and aerodynamic heating constraints are feasible options. From the set of feasible trajectories, one that maximizes delivered mass is a desired candidate. Alternatively, the mission designer may use a performance index based on a combination of time of flight and delivered mass.

Preliminary results indicate that a trajectory launching in February 2031, with a Jupiter flyby in June 2032, and arriving at Neptune in January 2039 is a promising candidate. The flight time is 7.87 years and the launch C_3 is 111 km^2/s^2. The launch capability of SLS Block 1B with kick stage is 6250 kg at the desired C_3 [29]. Trajectories to Neptune with flight times less than 13 years are infeasible with propulsive insertion [29,37], and hence the use of aerocapture with SLS allows a 5-year reduction in flight time. The high-energy trajectory with a fast arrival V_∞ of 20 km/s allows the use of a heritage blunt-body aeroshell with $L/D = 0.4$ if the TCW requirement can be lowered to about 1.25 deg as seen in Fig. 1. The expected peak heat rate is within the current tested capability of HEEET TPS [35]. The study emphasizes that these are preliminary estimates using engineering correlations for the convective and radiative heating rates [38]. The selected reference trajectory is used for analysis of the approach navigation errors and aerocapture performance analysis.

Upon arrival near the Neptune sphere of influence, the spacecraft targets the aim point on the B-plane to achieve the desired EFPA at atmospheric interface and the target orbit inclination [39]. Radiometric and optical navigation is used to guide the spacecraft to achieve the desired trajectory. Trajectory correction maneuvers (TCMs) are performed to reduce targeting errors as the spacecraft approaches the Neptune system. On exit from the atmosphere after aerocapture, the spacecraft coasts to an apoapsis of 400,000 km, and following a propulsive periapsis raise maneuver, it establishes the science orbit of 4000 km × 400,000 km. The target apoapsis altitude is chosen to be close to Triton's circular orbital radius. Two candidate inclinations for the science orbit to allow Triton flybys are 1) 157 deg retrograde with respect to Neptune, and 2) 23 deg prograde with respect to Neptune, which results in higher Triton encounter speeds compared with the prograde case. The retrograde entry results in higher planet-relative entry speeds and hence higher peak heat rate and heat load compared with the prograde entry.

Errors in the B-plane targeting translate to errors in EFPA at the atmospheric entry interface. Knowledge of the B-plane targeting uncertainty is critical to assessing aerocapture mission feasibility using low-L/D aeroshells. If the delivery error is beyond what the vehicle control authority can accommodate, the vehicle guidance control variable is saturated and the guidance algorithm is unable to achieve the desired capture orbit. Low-L/D blunt-body aeroshells offer less control authority than mid-L/D aeroshells, and can only accommodate smaller EFPA uncertainties compared with mid-L/D aeroshells. Accurate estimation of the navigation uncertainties along with atmospheric and other uncertainties is key to determining if blunt-body aeroshells offer sufficient control authority for Neptune aerocapture.
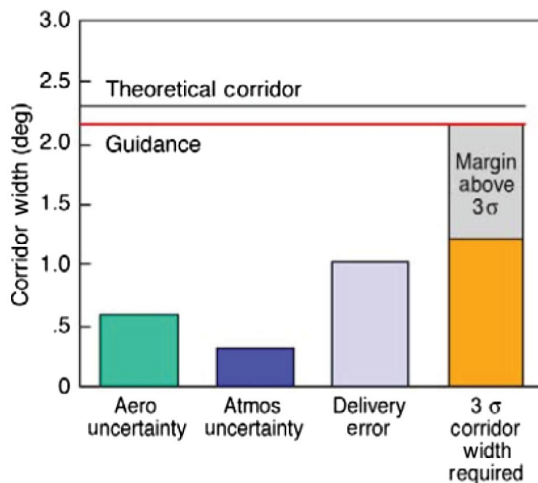

Fig. 2 Contribution of various uncertainties and root-sum-squared required corridor width for Neptune aerocapture as estimated by Lockwood et al. [1].

Delivery navigation error from spacecraft approach at Neptune was last quantified in 2004 by Lockwood et al. [1], and it is the dominant uncertainty component as seen in Fig. 2. Improvements in navigation techniques (higher-performance camera, refined ephemerides, etc.) could reduce the navigation uncertainty component and hence lower the vehicle L/D requirement. Atmospheric uncertainties at Neptune have been modeled in the Neptune Global Reference Atmospheric Model (Neptune-GRAM), but no improvements are available over the data used by Lockwood et al. [1]. Spilker et al. [4] recommend performing opportunistic stellar occultations of Uranus and Neptune to improve the atmospheric models, but they also note that the technique may provide information only at high altitudes and that extrapolating to altitudes relevant to aerocapture carries greater uncertainties. A dedicated research effort using Voyager data combined with new ground-based observations and modeling efforts may reduce the atmospheric uncertainties at altitudes relevant to aerocapture. Aerodynamic uncertainties have been quantified for a mid-L/D vehicle at Neptune during the 2004 systems analysis study [1], but no estimates are available for a low-L/D vehicle. A refined estimate of the delivery error is presented, along with a discussion of the current state of atmospheric and aerodynamic uncertainties.

The target orbit size and inclination are important parameters for both aerocapture and the subsequent tour of the Neptune system. The present study assumes a target capture orbit in Triton's orbital plane with apoapsis altitude nearly equal to Triton's orbital radius (400,000 km) and periapsis altitude around 4000 km. The basis of the assumption is that the ability to perform close targeted flybys of Triton will be a driver for a future Neptune mission. However, both larger and smaller capture orbits and other inclinations may be considered. For example, a highly elliptical orbit (apoapsis greater than about 1 million km) may be suitable for certain observations, whereas close-in circular orbits may be ideal for magnetic field or gravity science. Because highly elliptical orbits are prone to escape, the recommended option is to first aerocapture to a 400,000 km or lower apoapsis altitude orbit and then transfer to a higher orbit. Low circular orbits offer more corridor width and hence reduce the vehicle control requirement. However, low circular orbits also imply a short coast time to the first apoapsis where the periapsis raise maneuver must be performed. Previous studies using propulsive insertion have considered a retrograde target orbit to achieve low flyby speeds at Triton [29]. However, for aerocapture the retrograde entry heating rates are about five times greater compared with prograde entry as will be shown later in Sec. VIII. Hence from an aerothermal perspective a prograde capture orbit is favorable if the high flyby speeds do not compromise Triton science objectives. The mission designer must take into account all of the above tradeoffs and their implications of the target orbit on aerocapture feasibility, performance, and overall mission cost and complexity.

IV. Uncertainty Quantification

The aerocapture vehicle should have sufficient control authority to compensate for delivery error from approach navigation, atmospheric density uncertainties, and aerodynamic uncertainties. Quantification of these uncertainties is essential to evaluate the required vehicle L/D and is discussed in more detail in the following subsections.

A. Navigation Uncertainty

For the reference interplanetary trajectory, standard navigation covariance analysis is used to quantify the EFPA uncertainty at atmospheric entry interface (defined at 1000 km above the 1 bar pressure level). In this process, tracking data measurements are simulated along the reference trajectory and input into a linearized least-squares filter to estimate the spacecraft orbit and other parameters; the filter also produces a covariance matrix containing the uncertainties of the estimated parameters. Details of the navigation covariance analysis process are beyond the scope of this paper; a description of the data, methodology, and current state-of-the-art is available in the study by D'Amario and Watkins [40]. A high-level description and details relevant to the approach of Neptune are as follows.

For deep space missions, the tracking data include Doppler and range (which measure the line-of-sight velocity and distance of the spacecraft relative to a tracking station, respectively), and delta differential one-way ranging (ΔDOR), an interferometric data type in which the time delay of a radio signal from a spacecraft received at two tracking stations is used to compute an angular location of the spacecraft in the plane of sky. In addition, images of natural bodies taken by an onboard optical navigation (OpNav) camera provide a target-relative data type, especially important for approaching bodies whose orbit is not well known, such as Triton. The observable for OpNav data is the center of the observed body in the camera field of view (FOV) relative to the inertial pointing direction of the camera, computed through various centroiding techniques [41]. Because this is fundamentally an angular measure, the higher the angular resolution of the camera, the higher the accuracy of the OpNav data. The angular resolution is specified in terms of the angle extended by a single camera pixel, the instantaneous field of view (IFOV). For this study, two candidate optical navigation cameras are considered: 1) a generic medium-resolution (Mid-Res) camera with a relatively wide IFOV, and 2) a high-resolution (Hi-Res) camera with physical characteristics similar to the Long Range Reconnaissance Imager Camera (LORRI) flown on the New Horizons spacecraft. The camera specifications are shown in Table 1. Table 2 lists the 1σ noise on all the data types assumed in the analysis, and the tracking schedule for the radio and OpNav data.

The reference trajectory is obtained via numerical integration, with the force model including gravitational attraction from eight planets, the Neptunian moons Triton and Nereid, and the spherical harmonic gravity terms J_2, J_4 for Neptune. Four impulsive burns are also modeled, at Entry (E) - 30, 7, 5, and 2 days, and nally, small impulsive burns every 3 days are also included to account for minor spacecraft attitude adjustments. The nominal value for all burns in the reference trajectory is 0, but they are included in the filter so that their error is included in the estimated covariance. Of special note is the Neptune ephemeris; because errors in Neptune's position at arrival are a major driver of the navigation dispersion at entry, two cases were examined. The first case uses the current level of uncertainty in Neptune's orbit. The second case assumes that the uncertainty in Neptune ephemeris could be reduced by a factor of 100. The latter is a hypothetical improvement based on assumptions of future Neptune observations (private conversation with William Folkner, Jet Propulsion Laboratory, California Institute of Technology).

The integration of the reference trajectory, data simulation, and the estimation process is accomplished using the MONTE software

Table 1 Camera specifications

Camera	Specifications
Mid-Res	IFOV = 60 μrad
	FOV = 122 mrad
	Focal length = 500 mm
Hi-Res	IFOV = 5 μrad
	FOV = 5 mrad
	Focal length = 2619 mm

Table 2 Data tracking schedules and assumed noise

Data type	Tracking schedule	1σ noise
Doppler	3 × 8 h/week	0.1 mm/s
Range	3 × 8 h/week	3 m
ΔDOR	2 pairs/week	0.06 ns
OpNav	3 pictures/day	1 pixel

Triton OpNav begins at E-60 days.
Δ DOR = delta dierential one-way ranging.

Table 3   Estimated navigation filter parameters and uncertainties

Parameter	A priori 1σ uncertainty
Spacecraft state at epoch	$5E\text{-}4 \times 5E\text{-}4 \times 5E\text{-}4$ (km, Cartesian)
	$5E\text{-}1 \times 5E\text{-}1 \times 5E\text{-}1$ (km/s, Cartesian)
Neptune barycenter state	$2328 \times 790 \times 434$ (km, Cartesian)
	$3.2E\text{-}6 \times 4.2E\text{-}7 \times 1.3E\text{-}7$ (km/s, Cartesian)
Triton state	$5.8 \times 11.6 \times 8.4$ (km, Cartesian)
	$9.4E\text{-}5 \times 6.8E\text{-}5 \times 4.2E\text{-}5$ (km/s, Cartesian)
Nereid state	$180 \times 111 \times 108$ (km, Cartesian)
	$1.6E\text{-}5 \times 6.7E\text{-}6 \times 1.2E\text{-}5$ (km/s, Cartesian)
Impulsive maneuvers (E-30, E-7, E-5, E-2)	5 cm/s per axis
Small burns for repointing (every 3 days)	0.2 mm/s per axis
Neptune pole	Right ascension: 4.6E-2 deg
	Declination: 9.1E-3 deg
Neptune barycenter GM	$4.845 \text{ km}^3/\text{s}^2$
Neptune J_2, J_4	1.5E-6, 9.6E-7
Triton GM	$6.3E\text{-}1 \text{ km}^3/\text{s}^2$
Stochastic range biases at stations	2 m

Table 4   EFPA uncertainty of 1σ using current Neptune ephemeris

DCO, days	B-plane ellipse SMAA × SMIA, km	1σ |B| error, km	1σ EFPA error, deg
Only radiometric tracking, no OpNav			
E-09	328.8×255.3	272.9	1.78
E-07	327.5×254.2	271.3	1.77
E-04	325.1×253.3	270.3	1.76
With radiometric tracking and OpNav (Mid-Res)			
E-09	170.3×160.3	162.9	1.06
E-07	151.5×144.1	146.3	0.95
E-04	116.5×113.5	114.4	0.74
With radiometric tracking and OpNav (Hi-Res)			
E-09	39.8×35.4	39.2	0.26
E-07	30.5×26.9	30.1	0.20
E-04	17.6×14.6	17.1	0.11

SMAA = semi-major axis, SMIA = semi-minor axis.

set [42]. Typically, for deep space missions the estimated parameters include, in addition to the spacecraft state (position and velocity), dynamic parameters that affect the spacecraft orbit (such as ephemerides and gravity fields of nearby natural bodies), nongravitational forces acting on the spacecraft (such as solar radiation pressure and thrusting events), and parameters that affect the data (such as range biases). Also, some parameters are included in the filter as so-called considered parameters. These are bias parameters that contribute to the overall error covariance but are not estimated by the filter. They are typically used to account for parameters that are difficult to model or are poorly observed but are included in the covariance to prevent overly optimistic uncertainties. Examples of these are media propagation effects on the radio signal, and motion of the Earth's crust, which affects the location of the tracking stations. A complete list of standard filter parameters can be found in the paper by D'Amario and Watkins [40]; for the analysis performed in this study, Table 3 lists all the relevant ones, along with their a priori 1σ uncertainty.

The standard coordinate frame for the integration and estimation is the International Celestial Reference Frame, centered at Neptune, and the estimated state is provided in Cartesian coordinates at the beginning of the integration arc. For analyzing entry performance, however, the covariance estimate can be mapped forward in time and rotated into more suitable coordinates. One of these is the B-plane, which is a plane centered at the target body (Neptune in this case), and perpendicular to the incoming asymptote of the trajectory [43]. The mapped covariance is projected onto the B-plane as an ellipse, with the uncertainties represented by the major and minor axis of the ellipse. The covariance can also be mapped to the EFPA, and the EFPA error is proportional to the magnitude of the B-vector in the B-plane.

The 1σ EFPA uncertainty with current level of Neptune ephemeris is shown in Table 4. For the selected interplanetary trajectory with arrival $V_\infty = 20$ km/s, a vehicle with $L/D = 0.4$ entering prograde near the equator results in TCW ≈ 1.25 deg. If the $\pm 3\sigma$ navigation uncertainty alone exceeds the TCW, atmospheric and aerodynamic uncertainties cannot be accommodated. Preliminary simulations indicated that the 1σ delivery error cannot exceed 0.2 deg if a blunt-body aeroshell with $L/D = 0.40$ is used for the reference interplanetary arrival conditions. Table 4 shows that radiometric tracking alone (i.e., without OpNav) cannot achieve the desired delivery accuracy. Optical navigation using a Mid-Res camera with specifications listed in Table 1, along with radiometric navigation, is also unable to achieve the desired targeting accuracy. The Hi-Res camera significantly lowers the delivery error, and data cutoff (DCO) at E-07 meets the preliminary requirement and DCO at E-04 days exceeds it (the last two rows of Table 4). The delivery error for the E-04 DCO with current ephemeris uncertainty is considered baseline for the remainder of the

study. The EFPA errors for the scenario with 100 times improvement in Neptune ephemeris were similar to that obtained with the current Neptune ephemeris for E-07 and E-04 DCO. The calculations with the improved ephemeris did not produce a significantly different result and hence are not reported.

The result obtained using current Neptune ephemeris and the Hi-Res camera is an improvement over the previous estimate in literature, which was ± 0.17 deg (1σ) [1]. The smaller delivery error lowers the TCW requirement and hence the required L/D, as shown in Fig. 1. The results represent a preliminary assessment of the delivery uncertainties. Sources of error not considered in the study may inflate these uncertainties to some degree. The primary concern would be nongravitational effects on the spacecraft from mismodeled thrusting events, such as outgassing or momentum wheel desaturations. Other nongravitational effects [44] that were not considered in the study include solar radiation pressure, but at Neptune distances, this should be a small effect. Finally, systematic errors in OpNav centerfinding of extended bodies, such as Triton, may also degrade the results. Future studies with improved spacecraft system definition can refine the estimation of delivery uncertainties.

B.   Atmospheric Uncertainty

The large heliocentric distance presents a challenge to accurate measurement of Neptune's atmospheric characteristics. The Voyager 2 spacecraft remains the only spacecraft to provide a glimpse of the Neptune atmospheric profile during its flyby in 1989 [4,45]. Despite the limited data and the uncertainties in measurements, Neptune-GRAM is the state-of-the-art atmospheric model for aerocapture trajectory analysis. GRAMs are engineering level models for planetary atmospheres and are widely used for systems design and performance analysis of flight trajectories [1,46,47]. The atmosphere model implemented in Neptune-GRAM is based on the data from Voyager 2 radio science experiment, infrared interferometer-spectrometer, and ultraviolet spectrometer instrument [48]. Neptune-GRAM provides the density, temperature, pressure, winds, and chemical composition as a function of altitude, latitude, longitude, season, and local time. The model accounts for 1) uncertainty in analysis of Voyager data, 2) latitudinal variations in the atmospheric structure, and 3) temporal changes due to seasonal and diurnal variations [49].

Neptune-GRAM uses a single input parameter "Fminmax" to account for uncertainty and variability of the mean density profile. Fminmax $= -1$ corresponds to the minimum mean density and Fminmax $= +1$ corresponds to the maximum mean density as shown in Fig. 3. Neptune-GRAM recommends using Fminmax near 0 for near-equatorial entry at equinox, negative Fminmax for polar entry during winter, and positive Fminmax for polar entry during the summer. Neptune-GRAM also provides the expected $\pm 3\sigma$ variation of the mean profile about the selected Fminmax value as shown in Fig. 3. The full range of Fminmax along with the 3σ dispersion is expected to cover the worst-case uncertainty in mean density profile.
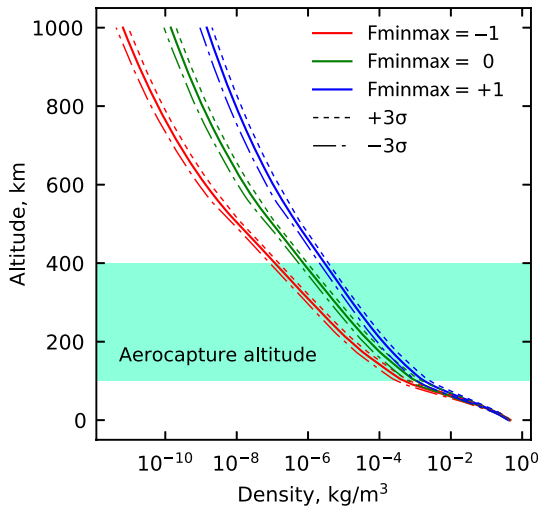
Fig. 3 Mean density profile variations from Neptune-GRAM by varying Fminmax from −1 to +1 and ±3σ uncertainties about the mean profiles.

For aerocapture at Neptune, knowledge of the density profile uncertainty is most important in the altitude range 100–400 km, which is referred to as the aerocapture altitude range. Aerodynamic forces are negligible above 400 km, and the minimum altitude during the aerocapture maneuver is well above 100 km for a wide range of vehicle L/D and arrival V_∞. Neptune-GRAM also provides high-frequency density perturbations superimposed on the mean profiles to account for random variations expected in the atmosphere as seen in Fig. 4. The parameter "rpscale" controls the high-frequency variability of the atmospheric density and ranges from 0 to 2, with 0 indicating no perturbations and 2 indicating the highest perturbation amplitude. Previous studies used a nominal value of rpscale = 1.0, and lower values such as 0.5 indicate lower high-frequency content. Previous studies have recommended using a smaller range of Fminmax depending on the arrival season and entry latitude instead of the full range. Lockwood et al. [1] used $0.60 \leq \text{Fminmax} \leq 0.93$ for an aerocapture vehicle flying in low latitudes in the season corresponding to the arrival time. The present study uses the full range of Fminmax from −1 to +1 as a worst-case estimate of the atmospheric uncertainties.

Better knowledge of the atmosphere from ground-based observations and modeling may reduce the atmospheric variability in terms
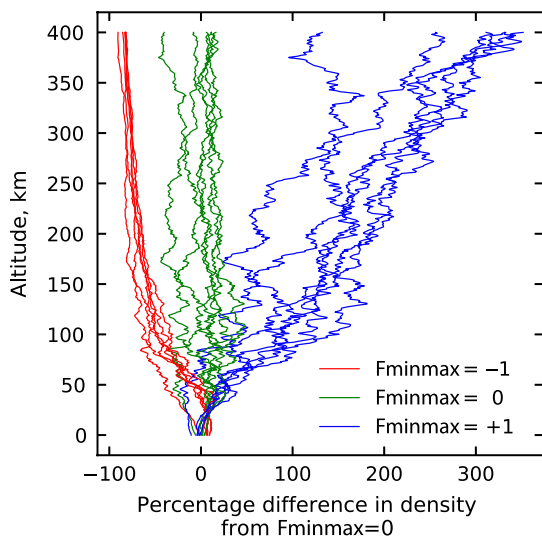
of both mean profile and high-frequency content. It is possible that existing observations when combined with global circulation models could constrain the range of Fminmax depending on the arrival season, and it is worth further investigation. The present study investigates a novel approach called a pathfinder probe recommended by Spilker et al [4]. An entry probe enters the atmosphere several weeks ahead of the main aerocapture vehicle and relays the in situ atmospheric density data. The aerocapture vehicle performs a TCM to adjust the target EFPA, and it is discussed in further detail in Sec. VII.

C. Aerodynamics Uncertainty

The vehicle aerodynamic control authority for bank angle modulation is quantified by the hypersonic trim lift-to-drag ratio $(L/D)_{\text{trim}}$ at the nominal trim angle of attack. Uncertainties in the mass distribution, ablation of the TPS material during aerocapture, shape changes, and mass imbalances translate into uncertainty in the vehicle $(L/D)_{\text{trim}}$. Quantification of aerodynamics uncertainties is important for entry vehicle performance analysis [50,51], but it is outside the scope of the present work. The present study uses a 10% 3σ dispersion about the nominal $(L/D)_{\text{trim}}$ as a representative estimate based on MSL entry vehicle aerodynamics reconstruction data [52]. Entry at Neptune presents a different and significantly more severe aerothermal environment than at Mars or Titan due to the higher entry speed and the H_2-He atmosphere. Additional study is required to quantify the aerodynamics uncertainties for a Neptune aerocapture vehicle using computational fluid dynamics and other numerical methods for prediction of TPS ablation during the maneuver.
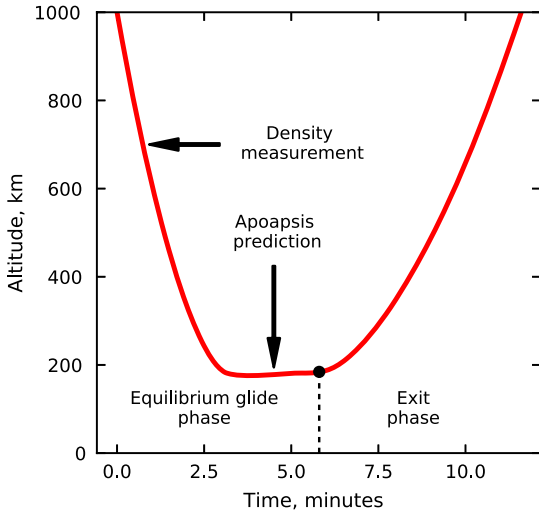
V. Guidance Scheme

The aerocapture guidance algorithm guides the vehicle from the entry interface through atmospheric flight such that a desired set of terminal conditions is achieved when the vehicle exits the atmosphere. The desired terminal conditions at atmospheric exit allow the spacecraft to achieve the target capture orbit apoapsis and inclination. The present work uses bank angle modulation as the control method. Bank angle modulation uses an aeroshell that provides lift from offsetting the center of gravity with respect to the symmetry axis. The lift vector is rotated around the velocity vector by banking the vehicle, and the bank angle is the sole control variable. Bank angle modulation has been successfully used on entry vehicles such as Apollo and the MSL, and it is considered a high-heritage flight control technique for low-L/D blunt-body aeroshells [53,54]. The guidance scheme used in the present work is a derivative of the analytical predictor-corrector developed by Cerimele and Gamble [55]. The guidance consists of two phases: 1) the equilibrium glide phase, and 2) the exit phase as shown in Fig. 5. In the equilibrium glide phase, the vehicle attempts to maintain equilibrium glide condition, i.e., altitude acceleration $\ddot{h} = 0$. The bank angle command δ_{CMD} during the equilibrium glide phase is computed as [55]

$$\cos \delta_{\text{CMD}} = \cos \delta_{\text{eq.gl.}} - G_{\dot{h}} \dot{h} + G_{\bar{q}} \left(\frac{\bar{q} - \bar{q}_{\text{ref}}}{\bar{q}} \right) \qquad (1)$$

where $\cos \delta_{\text{eq.gl.}}$ is the calculated equilibrium glide bank angle to which increments are added, and it is given by [55]

$$\cos \delta_{\text{eq.gl.}} = \frac{mg}{C_L \bar{q} S} \left(1 - \frac{v^2}{gr} \right) \qquad (2)$$

where m is the vehicle mass, g is the local gravitational acceleration, C_L is the vehicle lift coefficient, $\bar{q}$ is the dynamic pressure, S is the aerodynamic reference area, v is the atmosphere relative speed, and r is the radial distance from the center of the planet. $G_{\dot{h}}$ and $G_{\bar{q}}$ refer to the gain parameters and are chosen based on the method developed by Cerimele and Gamble [55] described in Appendix A. The reference dynamic pressure $\bar{q}_{\text{ref}}$ is computed as [55]
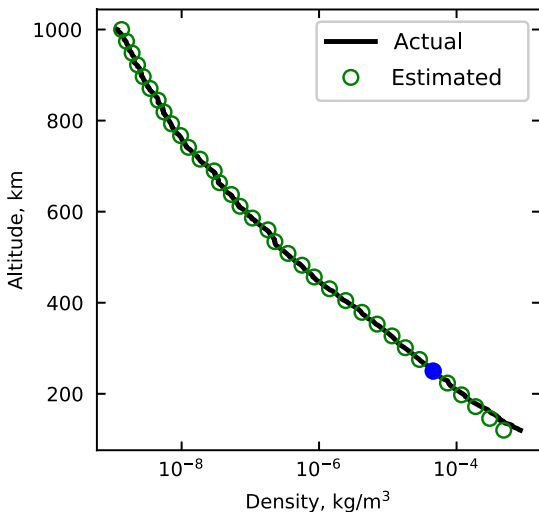

Fig. 4   Random perturbed density profiles from Neptune-GRAM for different values of Fminmax [1].

Fig. 5 Altitude history of the aerocapture maneuver showing the equilibrium glide phase and exit phase of the guidance algorithm.

$$\bar{q}_{\text{ref}} = -\frac{mg}{0.75 C_L S}\left(1 - \frac{v^2}{gr}\right) \qquad (3)$$

A key feature of the guidance algorithm proposed in the present work is the onboard density estimation during the descending leg of the aerocapture maneuver. The vehicle uses the accelerometer measurements to estimate the atmospheric density during the equilibrium glide phase until a predetermined altitude rate $\dot{h}$ is exceeded.

$$\rho_{\text{est}} = \frac{2 m a_{\text{drag}}}{S C_D v^2} \qquad (4)$$

where ρ_{est} is the estimated density, a_{drag} is the measured drag acceleration, and C_D is the drag coefficient. The present study assumes that the drag deceleration can be accurately estimated from onboard accelerometer readings [56,57]. Figure 6 shows the comparison of actual and estimated density profiles for a vehicle with $L/D = 0.4$ entering Neptune retrograde equatorial at 33 km/s (planet-relative speed) and accelerometer measurement frequency of 2 Hz. For altitudes below the minimum altitude at which density measurements are available, the algorithm extrapolates the density using an exponential model. The extrapolation uses the density estimate and computed

scale height at the minimum altitude at which a measurement is available. The blue circle in Fig. 6 indicates the minimum altitude at which measurement was available, beyond which the profile is extrapolated. Figure 7 shows the percentage error in density estimation as a function of altitude. Potential sources of error in the density measurement such as data noise, uncertainty in vehicle mass, and speed are not considered in the present study. The effect of turbulent buffeting, data noise and filtering, sensor response time, and computational cost of constructing a reliable density function using onboard computing resources are beyond the scope of the present work.

Although onboard density estimation is proposed by many studies addressing aerocapture at Mars [57–59], its application to Neptune aerocapture has not been studied. Onboard density estimation significantly improves the guidance performance compared with using a preset density profile, and it is of critical importance to aerocapture at Neptune due to low TCW compared with Mars or Titan. Encountering a higher-than-expected-density atmosphere could result in failure due to undershooting of the target apoapsis; a less-dense atmosphere can result in apoapsis overshoot. Worst-case scenarios involving low-density atmosphere can result in the spacecraft leaving the atmosphere without getting captured. The proposed guidance scheme is shown to be able to achieve satisfactory performance even with large atmospheric uncertainties as shown in Sec. VIII.

Once a predetermined altitude rate $\dot{h}$ threshold is exceeded, the vehicle starts predicting its apoapsis altitude at exit using full lift up for the remainder of the atmospheric flight. The prediction is done by numerically integrating the equations of motion using the density profile measured during the descending leg of the aerocapture maneuver as shown in Fig. 5. When the predicted apoapsis altitude at exit is sufficiently close to the desired value, the exit phase is initiated and the vehicle pulls out of the atmosphere with full lift up for the remainder of the atmospheric flight. Density pockets and density shears are not modeled in Neptune-GRAM and may be a concern for aerocapture vehicles [60]. A case for concern would be if the density pockets are localized, and not encountered by the vehicle during the descending leg but only during the ascending leg resulting in erroneous apoapsis prediction. Further study is required to investigate the magnitude and spatial extent of density pockets in ice giant atmospheres and their effect on aerocapture performance.

The bank angle commanded to target the desired apoapsis will result in an out-of-plane force component for bank angles other than 0 deg (lift up) or 180 deg (lift down). The out-of-plane force component will cause the inclination to change as the vehicle flies through the atmosphere. Because bank angle is the only control available to target the apoapsis at both exit and inclination, the strategy adopted is to perform bank angle reversals when the inclination exceeds prescribed bounds [55]. Because the maximum roll rate is limited, the

Fig. 6 Comparison of an actual perturbed random profile from Neptune-GRAM and estimated density profile from measured drag deceleration.
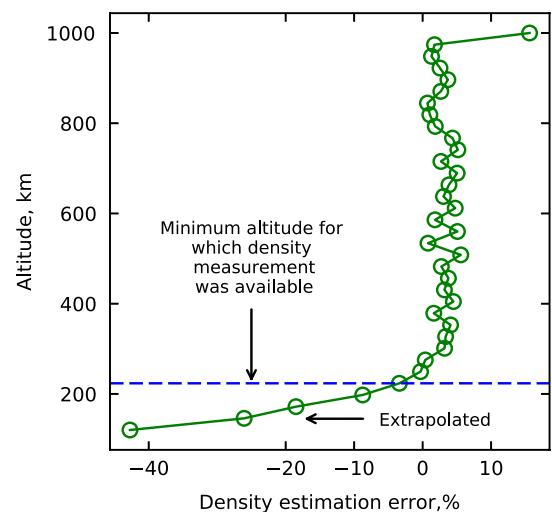
Fig. 7 Density estimation error. Below the minimum altitude for which onboard measurements are available, an exponential extrapolation is used.

vehicle will take a few seconds to complete the roll reversal and lead to some error in apoapsis targeting. The present study focuses only on the apoapsis targeting and leaves the inclination unconstrained for simplicity. Inclination errors from the atmospheric pass are expected to be small and can be corrected along with the periapsis raise maneuver. Additional study is required to include inclination targeting in the proposed guidance scheme and analyze its effect on apoapsis targeting accuracy.

VI. Hybrid Propulsive-Aerocapture Concept

The hybrid propulsive-aerocapture concept refers to a technique where rocket propulsion provides a component of the deterministic ΔV for orbit insertion along with aerocapture. Using a combination of aerocapture and propulsion has been suggested as a method to reduce the vehicle L/D requirement for ice giant missions by Spilker et al. [4]. The present work considers two hybrid approaches that showed the potential to enable use of low-L/D blunt-body aeroshells at Neptune.

The first approach involves aerocapture into an initial orbit with apoapsis lower than the planned science orbit, and then propulsively boosting the apoapsis to the desired orbit. The small initial capture orbit widens the theoretical corridor (TCW) and hence lowers the required vehicle L/D. An additional advantage of a small initial orbit is that it reduces the risk of accidental escape following aerocapture. The primary performance penalty for this hybrid approach is the propulsive ΔV cost for the apoapsis raise maneuver, as a high propulsive ΔV implies significant mass penalty. Additional risks from a small capture orbit include 1) increased ring plane crossing hazard (particularly if the initial apoapsis is close to or inside the rings), and 2) less available time for orbit determination and corrective maneuvers compared with large orbits that have a several day coast period to the first apoapsis. Figure 8 shows the effect of initial capture orbit period on vehicle L/D requirement. The TCW constraint lines show the 2.0 deg contours for a range of initial capture orbits. The analysis assumes that the desired science orbit has a 20-day period with a periapsis radius of 1.1 Neptune radius. The green-shaded patch shows the feasible set of $(L/D, V_\infty)$ if the initial capture orbit is 20 days. If a smaller one-day capture orbit is used, the blue patch becomes feasible, lowering the L/D requirement. After the periapsis raise maneuver, an apoapsis raise maneuver is performed at the periapsis.

Table 5 shows the minimum required L/D using different capture orbits for arrival at $V_\infty = 20$ km/s, and the apoapsis raise ΔV cost to achieve the 20-day science orbit. Using a small capture orbits does lower the L/D requirement (but not significantly to enable use of low-L/D aeroshells with reasonable ΔV penalty). Capture orbits less than 1 day incur prohibitively high apoapsis raise ΔV and ring plane

Table 5 Minimum required L/D and deterministic propulsive ΔV cost for hybrid aerocapture-propulsive approach using small initial capture orbits, $V_\infty = 20$ km/s, target science orbit period = 20 days

Initial capture orbit period, days	Initial apoapsis altitude, km	$(L/D)_{min.}$	Apoapsis raise ΔV, m/s
20	1,553,575	0.61	0
1	166,163	0.51	1,252
0.5	85,543	0.45	2,148
0.25	34,755	0.38	3,658

crossing hazard due to the low initial apoapsis. ΔV of 2 km/s or greater begin to approach the value for purely propulsive insertion, and accommodation of large propellant tanks inside an aeroshell presents another challenge.

The second hybrid approach involves aerocapture followed by a propulsive ΔV maneuver immediately after atmospheric exit as shown in Fig. 9. The propulsive ΔV capability allows a wider of range of EFPAs than conventional aerocapture and hence increases the TCW. $TCW_{\Delta V}$ indicates the modified TCW with the additional ΔV and is equal to the TCW for conventional aerocapture when $\Delta V = 0$. The ΔV corrects for the deficit in speed for a steeper entry than aerocapture and corrects for excess speed in the case of a shallower entry than possible with aerocapture alone. The propulsive ΔV thus augments control authority and may allow reduction in vehicle L/D requirement. As with the first approach, the primary penalty for this approach is the propellant mass associated with the ΔV maneuver. In addition, the spacecraft has to autonomously determine its orbital state, compute the correction maneuvers, and execute the propulsive burn without any ground intervention immediately after atmospheric exit.

Figure 10 shows the effect of additional propulsive ΔV on the required vehicle L/D. The TCW constraint lines show the 2.0 deg contours for a range of allowable propulsive ΔV. The green-shaded area shows the feasible set of $L/D, V_\infty$ for conventional aerocapture with no ΔV maneuver at exit. If a propulsive ΔV maneuver of 1 km/s is allowed, the blue patch becomes feasible in addition to the green area, lowering the L/D requirement. After the ΔV maneuver is performed, the vehicle has the correct speed to coast to the target apoapsis and following a periapsis raise maneuver enters the desired science orbit.

Table 6 shows that the additional propulsive ΔV capability widens the theoretical corridor and thus lowers the L/D requirement. However, the reduction in required L/D is small and is not sufficient to enable the use of low-L/D aeroshells within a reasonable ΔV of 1 km/s. The propulsive ΔV required to allow use of heritage aeroshells is prohibitively high and leads to unacceptable propellant mass penalty for this hybrid propulsive-aerocapture concept. The propellant mass penalties outweigh the performance benefits and likely introduce additional cost and complexity.
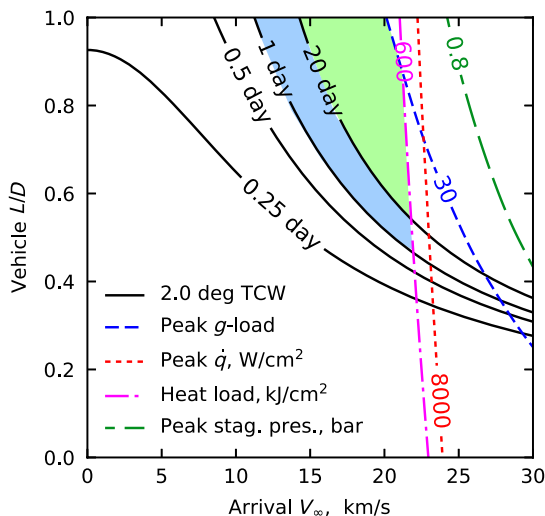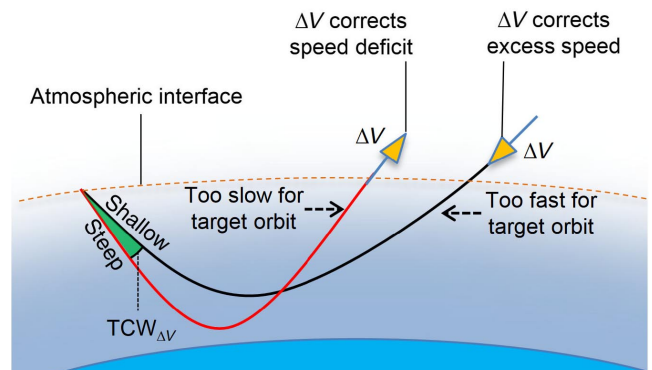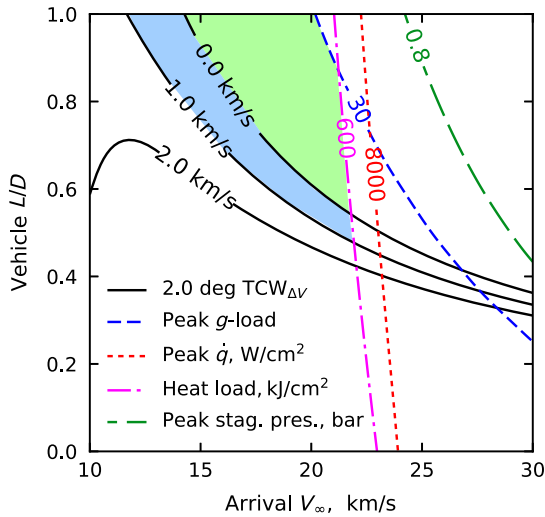

Fig. 8 Effect of initial capture orbit period on vehicle L/D requirement. Shaded regions show the feasible set of $L/D, V_\infty$ for 20-day and 1-day capture orbits.

Fig. 9 Second approach where a propulsive ΔV at atmospheric exit augments control authority.

Fig. 10 Feasibility chart showing the effect of allowable propulsive ΔV at exit on vehicle L/D requirement.

Fig. 11 The colored blocks show the theoretical corridor for various mean density atmospheric profiles. The target EFPA is chosen to minimize the risk of escape.

Table 6   Minimum required L/D for hybrid propulsive-aerocapture approach with a propulsive ΔV maneuver at atmospheric exit, $V_\infty = 20$ km/s, target science orbit period = 20 days

Allowable propulsive ΔV, km/s	$(L/D)_{\min.}$
0.0	0.61
0.5	0.58
1.0	0.54
1.5	0.51
2.0	0.47

VII.   Pathfinder Probe Concept

The present study investigated the option of sending a pathfinder entry probe into Neptune's atmosphere several weeks ahead of the main aerocapture vehicle reaching the atmospheric entry interface. The objective of the pathfinder probe is to measure the in situ atmospheric profile and thus reduce the uncertainty in atmospheric profile before the aerocapture vehicle arriving at Neptune. Before the discussion of the pathfinder probe concept, it is insightful to discuss the "targeting problem" for aerocapture to illustrate the combined effect of navigation and atmospheric uncertainties. The targeting problem refers to the selection of a nominal target EFPA for the aerocapture maneuver. Several weeks ahead of entering Neptune, the approach navigation maneuvers target the aim point on the B-plane to allow the spacecraft to reach the atmospheric interface at the selected nominal EFPA.

The TCW is bounded by the shallowest and steepest acceptable EFPA for aerocapture. Figure 11 shows the TCW for a vehicle with $L/D = 0.4$ entering Neptune's atmosphere retrograde at the equator at a planet-relative speed of 33 km/s for Fminmax $= -1, 0$, and $+1$. These values of Fminmax correspond to the minimum, average, and maximum mean density profiles from Neptune-GRAM. Theoretically, if the vehicle enters at any EFPA within the TCW, the guidance algorithm can command the appropriate bank angle profile to achieve the desired exit conditions. However, simulations indicate that entry near the shallow limit of the corridor that requires almost full lift down for the entire trajectory are very sensitive to density perturbations. Such full lift down trajectories are not flyable in practice due to the risk of flyaway without getting captured. The hatched regions in Fig. 11 show the portion of the corridor rendered inaccessible due to the sensitivity of trajectories near the shallow limit using the guidance algorithm described in Sec. V and parameters listed in Appendix A. Thus the usable corridor for Neptune aerocapture is smaller than the theoretical corridor. Though the width of the corridor is not very
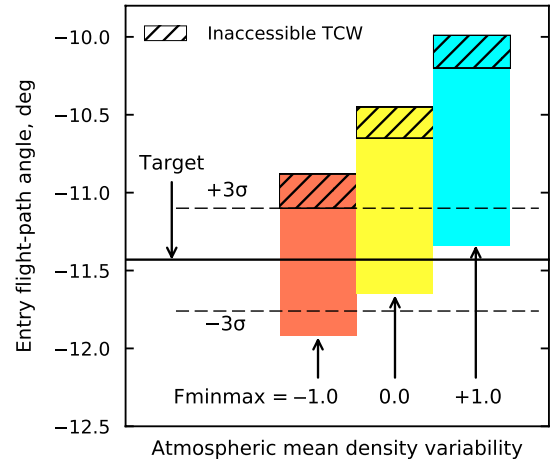
sensitive to Fminmax, the shallow and steep bounds of the usable corridor change significantly based on the mean density profile and lead to the targeting problem. The selected nominal EFPA should be such that the $\pm 3\sigma$ navigation uncertainty falls within the usable corridor for the entire range of mean density profile uncertainties. Targeting the selected nominal EFPA allows the aerocapture vehicle to achieve the desired exit conditions for any mean atmospheric profile within the specified uncertainty.

In the present study, it is seen that a 3σ EFPA uncertainty of 0.33 deg (see Table 4) shown in Fig. 11 is not small enough to accommodate the entire range of mean density profiles from Fminmax $= -1$ to $+1$. There is no target EFPA that would allow both the $+3\sigma$ and -3σ delivery error to fall within the usable corridor for the range of atmospheric uncertainties considered. If the vehicle encounters the lowest density atmosphere (i.e., Fminmax $= -1$) and the EFPA falls outside $+3\sigma$, then the vehicle risks not getting captured. To minimize the risk of escape, the target EFPA is chosen such that the $+3\sigma$ delivery error falls just within the usable corridor for the minimum density atmosphere. For the case with the maximum density atmosphere (i.e., Fminmax $= +1$), the target EFPA itself and the -3σ delivery error fall below the theoretical corridor, which implies that the vehicle will undershoot the apoapsis altitude in such a scenario.

Simulations indicate that off-nominal EFPA outside $+3\sigma$ is very likely to fly away without getting captured, whereas off-nominal EFPA outside -3σ will only likely result in undershoot of apoapsis but certainly not crash into the planet. The flyway case will almost certainly lead to loss of mission, whereas the apoapsis undershoot can be corrected using propulsive maneuvers and Triton gravity assists during the course of the mission. It is recommended to bias the target EFPA toward the steep side of the usable corridor to provide sufficient safety margin against the flyaway scenario for minimum density atmosphere, even if the -3σ EFPA bound falls outside the usable corridor for the maximum density atmosphere. Two possible options to increase the safety margin are 1) to decrease the navigation uncertainties further, and 2) to reduce the atmospheric uncertainties. The pathfinder probe concept aims to use the second option of reducing atmospheric uncertainties to improve the safety margin against accidental escape.

The concept of operations for the pathfinder probe is as follows. Ahead of the main aerocapture vehicle reaching Neptune, an atmospheric entry probe is released from the main spacecraft. The carrier spacecraft also releases one or more SmallSats on a flyby trajectory with their arrival timed so as to act as a data relay from the probe during entry. The probe coasts to Neptune, whereas the main spacecraft performs a small propulsive burn such that it arrives at entry interface for aerocapture a few weeks after the probe entry. The probe measures the density in situ (from accelerometer measurements), along with atmospheric structure and composition. The data are
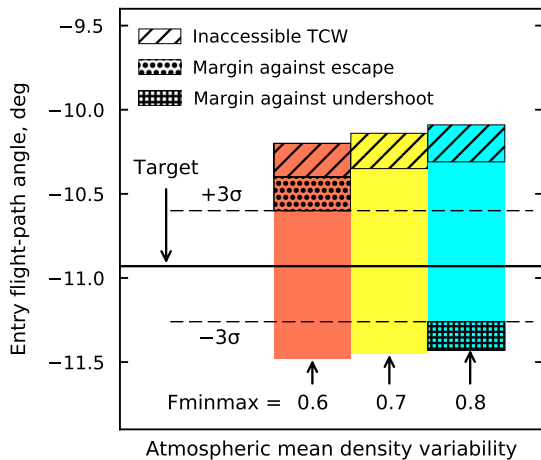
Fig. 12 Reduced atmospheric uncertainty from a pathfinder probe allows target EFPA selection such that both $+3\sigma$ and -3σ delivery errors fall within the usable corridor.

relayed to the main spacecraft via the SmallSats, which in turn relay the data back to Earth. The present study hypothesizes that the in situ data when coupled with improved atmospheric models and ground-based observation campaigns can reduce the uncertainty in the mean density profile to be encountered by the main aerocapture vehicle. The aerocapture vehicle then performs a small TCM to target the optimal EFPA based on the improved atmospheric profile knowledge.

Quantification of the atmospheric uncertainty reduction from a pathfinder entry probe is not possible at the level of the study. For illustration, the present study assumes that the pathfinder probe data are able to constrain the atmospheric uncertainties such that $0.6 \leq$ Fminmax ≤ 0.8 instead of the full range of Fminmax from -1 to $+1$. With the reduced uncertainty in Fminmax, the target EFPA can be chosen so as to provide sufficient margin against escape above 3σ in the case of low-density atmosphere, and against undershoot in the case of high-density atmosphere as shown in Fig. 12. The pathfinder probe allows optimal selection of the target EFPA to minimize the risk of accidental escape or apoapsis undershoot. The pathfinder probe can improve the safety margin for aerocapture against escape and undershoot scenarios. Constraints on the timing of probe and SmallSat release, data transmission from the probe, propulsive ΔV for deflection maneuvers, the time available for data analysis, and command upload to spacecraft for targeting the optimal EFPA are recommended for further study. It may be possible to let the relay SmallSat carry the pathfinder probe, and the SmallSat separate several months ahead of the main spacecraft reaching Neptune to keep the deflection maneuver ΔV reasonably low. If the two spacecraft can separate before the Jupiter gravity assist, it may be possible to further reduce the required deflection ΔV to achieve the few weeks' separation between the pathfinder probe and the main spacecraft reaching Neptune; however, this will add significant complexity to the mission architecture and spacecraft systems.

Inclusion of a pathfinder probe (in addition to a main entry probe) will add cost and complexity to the mission architecture. The design of the pathfinder probe is not part of the study and assumes that the

primary mission can accommodate the additional mass. The possibility of the pathfinder probe failing to accomplish its mission should be considered, due to entry probe failure, loss of data, etc. Loss of the pathfinder probe cannot be a single point failure for the main aerocapture vehicle and should be capable of performing the maneuver with sufficient safety margin even if the data from the pathfinder probe is lost.

In the following section on performance analysis, the hybrid aerocapture approaches in Sec. VI are not considered further. The improved navigation uncertainty estimates from Sec. IV, the guidance scheme with onboard density estimation from Sec. V, and the use of a pathfinder probe from Sec. VII are considered for aerocapture performance analysis using a blunt-body aeroshell.

VIII. Performance Analysis

Monte Carlo analysis is used to quantify the vehicle performance in the presence of combined navigation, atmospheric, and aerodynamic uncertainties. Nominal values of the parameters used and the associated uncertainties are listed in Table 7. The target EFPA is chosen based on the discussion presented in Sec. VII. For arrival $V_\infty = 20$ km/s of the reference interplanetary trajectory, the planet/atmosphere relative entry speed can range from 28 km/s for prograde entry to 33 km/s for retrograde entry. The location and width of the entry corridor change as a function of the planet-relative entry speed and must be accounted for in aerocapture guidance analysis. The arrival declination is 8.8 deg, and the entry latitude and heading angles can be computed based on the target orbit inclination [39]. The heading angle is defined as the angle between the velocity vector and the local parallel of latitude following the definition of Vinh et al. [61]. To simplify the trajectory analysis, the aerocapture simulations in this study use equatorial retrograde (180 deg heading angle) and prograde (0 deg heading angle) entry. The apoapsis altitude is computed using the trajectory state at atmospheric exit, defined at the same altitude as the entry interface (1000 km above the 1 bar pressure level). Atmospheric mean density uncertainties and random high-frequency perturbations are used from Neptune-GRAM. Three sets of simulations were performed: 1) maximum range of Fminmax, 2) reduced atmospheric uncertainty, and 3) very low atmospheric uncertainty.

A. Maximum Range of Fminmax

The maximum atmospheric uncertainty case assumes that no improvement is available over data available from Neptune-GRAM, and the aerocapture vehicle must accommodate the full range of Fminmax from -1 to $+1$.

Vehicle parameters used for the simulation are ballistic coefficient $\beta = 200$ kg/m^2, drag coefficient $C_D = 1.59$, and nose radius $R_N = 1.0$ m. The target apoapsis altitude is 400,000 km, and the apoapsis error tolerance used by the guidance algorithm is 10,000 km. The apoapsis prediction is initiated when the altitude rate exceeds -500 m/s and a guidance frequency of 2 Hz is used for the equilibrium glide phase. The onboard density estimation assumes perfect knowledge of the total measured acceleration and other vehicle parameters and computes the density once during every guidance cycle. Guidance gain parameters used in the simulation are described in Appendix A. If the guidance algorithm predicts

Table 7   Monte Carlo uncertainties

Category	Variable	Nominal	$\pm 3\sigma$ or [min, max] or other	Distribution
Navigation	Entry flight-path angle (planet-relative)	-11.43 deg (retrograde)	± 0.33 deg	Normal
		-13.85 deg (prograde)	± 0.33 deg	Normal
Atmosphere	Fminmax	— —	$[-1, +1]$	Uniform
	Mean density uncertainty	0	3σ from Neptune-GRAM	Normal
	Random high-frequency perturbation	— —	rpscale $= 1$	Uniform
Aerodynamics	L/D	0.40	± 0.04	Uniform

an apoapsis altitude lower than the target value, the equilibrium glide phase is terminated immediately and the vehicle flies full lift up. Higher guidance frequency can improve the apoapsis targeting, although at the cost of greater onboard computing requirements. Vehicle position and velocity states used by the guidance scheme will have uncertainties associated with inertial sensors but for the present study are assumed to be known perfectly. The maximum roll rate is constrained to 30 deg/s. Orbit inclination targeting during the aerocapture maneuver is not considered.

A high-fidelity 3-degree-of-freedom simulation including gravity zonal harmonics up to J_4, aerodynamic forces, Coriolis, and centrifugal forces is used to simulate the trajectory of a spacecraft flying in the vicinity of an oblate, rotating planet. The initial state for the entry simulation is the terminal state of the interplanetary approach trajectory using the B-plane targeting method [39]. The aerocapture trajectory is propagated from atmospheric entry to the atmospheric exit interface. The simulation uses an outer loop to propagate the actual vehicle trajectory and an inner loop to simulate the guidance scheme. Five thousand aerocapture trajectories were simulated for both prograde and retrograde entry for different atmospheric uncertainty levels, and the results are used to assess guidance performance at Neptune using a blunt-body aeroshell.

1. Retrograde Entry

For the purpose of comparing the targeting accuracy for different cases evaluated, an arbitrary ±50,000 km bound about the target apoapsis is defined in this study. For the retrograde entry, all but one of the 5000 cases captured successfully, with 75% of the cases achieving apoapsis within ±50,000 km of the target apoapsis (400,000 km). Figure 13 shows the histogram of the achieved apoapsis altitude. Figure 14 shows the dispersion in apoapsis and periapsis altitude. One trajectory failed to capture and is omitted from Figs. 13 and 14. The failure is attributed to low mean density (i.e., Fminmax = −1.0), −0.4σ variation about the mean profile, and shallow EFPA = −11.02 deg (+3.7σ) along with the effect of high-frequency perturbations.

Figure 15 shows the dispersion in peak deceleration and peak stagnation-point heat rate. The stagnation point heat rate is the sum of convective and radiative heating rates computed using engineering correlations [38]. The 99.87-percentile peak deceleration load is 14.32g, an important parameter for aeroshell structural design and instrument qualification. The 99.87-percentile peak stagnation-point heat rate is 8152 W/cm², an important parameter for TPS material selection and qualification. The heat rate is significantly higher compared with entry at Mars or Titan, but it is expected to be within the performance envelope of the HEEET TPS [35]. The
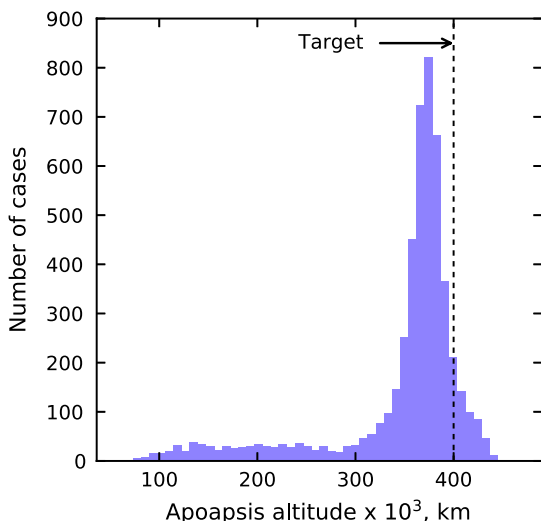

Fig. 14 Apoapsis dispersion for maximum range of Fminmax (retrograde). Of the cases, 75% achieved apoapsis within 50,000 km of the target.

Fig. 15 Peak deceleration and peak stagnation-point heat rate for maximum range of Fminmax (retrograde).

Fig. 13 Histogram of achieved apoapsis altitude for maximum range of Fminmax. Some cases resulted in significant undershoot (below 300,000 km).

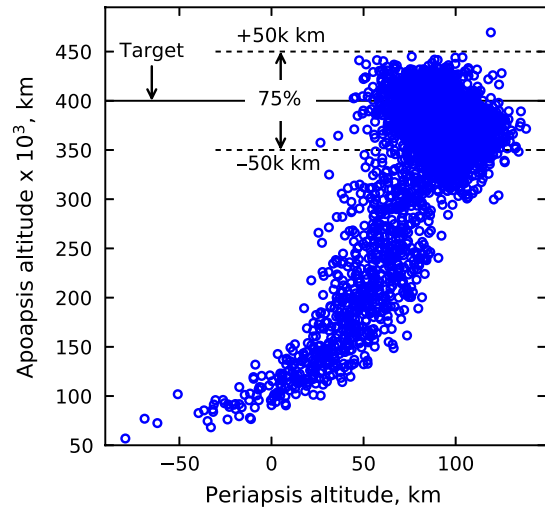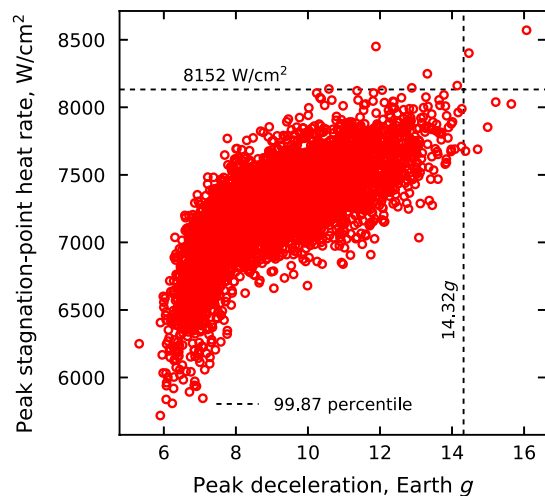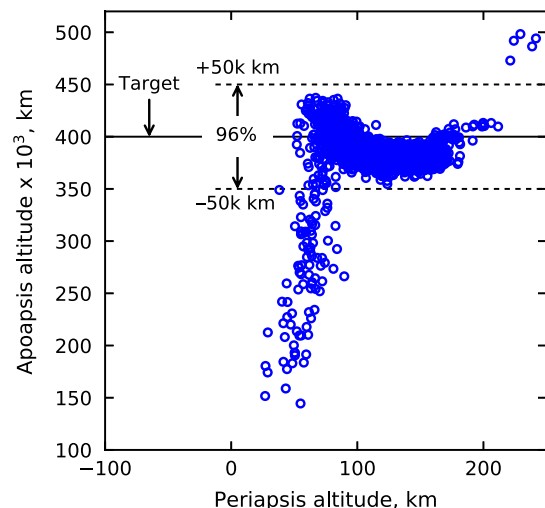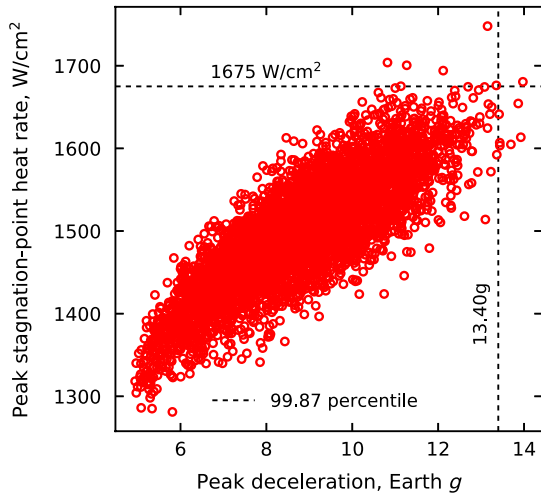**Fig. 16 Apoapsis versus periapsis altitude for maximum range of Fminmax (prograde). Of the cases, 96% achieved apoapsis altitude within 50,000 km of the target.**

Fig. 17 Peak deceleration versus peak stagnation-point heat rate for maximum range of Fminmax (prograde). Note the reduction in heat rate compared with retrograde entry (Fig. 15).

99.87-percentile propulsive ΔV requirement for the periapsis raise and the apoapsis correction maneuver are 315 and 1841 m/s, respectively. The high apoapsis correction ΔV is due to a significant fraction of the cases undershooting the target apoapsis. The apoapsis undershoot in turn is attributed to selection of the target EFPA so as to minimize the risk of escape in the event of minimum density atmosphere as described in Sec. VII. In the event of high-density atmosphere, the nominal target EFPA results in apoapsis undershoot. The study emphasizes that the reported apoapsis correction ΔV values are strongly dependent on the 400,000 km target apoapsis. This is based on the study ground rule that Triton is a high-priority science target for a future Neptune mission [29], and the orbit should be large enough to permit close Triton flybys. If a future mission chooses to forego this requirement to use a much smaller target apoapsis, the apoapsis correction ΔV values will be much smaller. The apoapsis correction ΔV values are also reported to compare the cost of correcting targeting errors for the different atmospheric uncertainty levels and vehicle L/D values considered in this study.

2. Prograde Entry

For the prograde entry, 98.48% of the cases captured successfully; 0.70% of the cases captured but with apoapsis altitudes greater than 500,000 km; 96% of the cases achieved apoapsis within ±50,000 km of the target apoapsis (400,000 km). Figure 16 shows the dispersion in apoapsis versus periapsis altitude. The trajectories that failed to capture and those that resulted in apoapsis altitude greater than 500,000 km are omitted from Fig. 16.

Figure 17 shows the dispersion in peak deceleration and peak stagnation-point heat rate. The 99.87-percentile peak deceleration load and stagnation-point heat rate are 13.40g and 1675 W/cm^2, respectively. The 99.87-percentile stagnation-point heat rate for prograde entry is substantially lower than the retrograde entry case due to the lower planet-relative entry speed for prograde entry. The 99.87-percentile propulsive ΔV requirement for the periapsis raise maneuver and apoapsis correction maneuver is 180 and 664 m/s, respectively. Compared with the retrograde entry case where only 0.02% of the cases failed to capture, 1.5% of the cases failed to capture in the prograde case. Despite the lower capture probability, the fraction of cases that achieved apoapsis within ±50,000 km for the prograde case is 96% compared with 75% for the retrograde case. The cases that failed to capture or resulted in large orbits are attributed to combinations of shallow EFPAs and low-density atmosphere. Table 8 summarizes the percentiles for various parameters from Monte Carlo simulations with the full range of Fminmax.
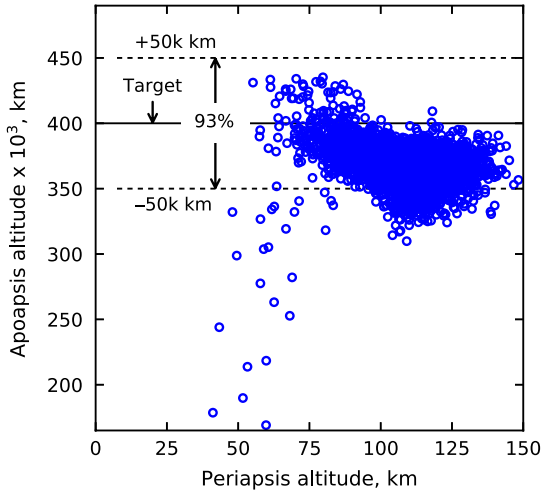
B. Reduced Atmospheric Uncertainty

To investigate the effect of reduced atmospheric uncertainty from potential ground-based observations and modeling efforts, the simulation is run with $-0.5 \leq$ Fminmax $\leq +0.5$, and rpscale = 0.5. Other simulation parameters are the same as listed in Table 7. The results are reported for retrograde and prograde entry.
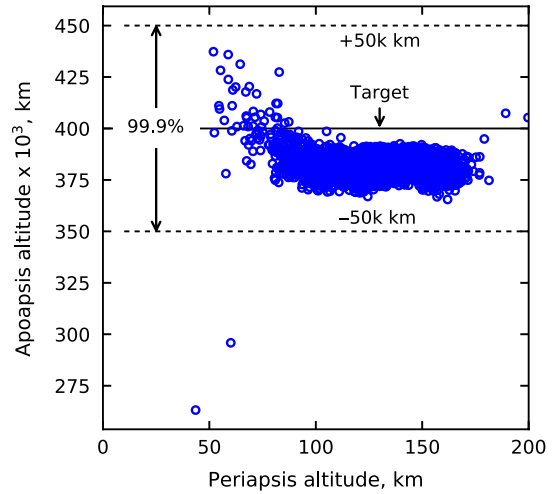
1. Retrograde Entry

One hundred percent of the cases captured successfully. The percentage of cases that achieved apoapsis within ±50,000 km of the target is 93% as shown in Fig. 18 compared with 75% for the simulations with maximum atmospheric uncertainty. The improved apoapsis targeting lowers the 99.87-percentile apoapsis correction ΔV from 1840 (Table 8) to 328 m/s. Table 9 summarizes the Monte Carlo simulation results for the retrograde entry case.

Table 8   Statistics from Monte Carlo simulation with full range of Fminmax

Retrograde entry				
Percentage captured			99.98	
Percentage within ±50,000 km of target			74.94	

Statistics for the 99.98% cases captured					
Parameter	Minimum	0.13 percentile	Median	99.87 percentile	Maximum
Apoapsis altitude, km	56,869	77,399	369,681	441,215	469,411
Peak deceleration, Earth g	5.32	6.00	9.01	14.32	16.07
Peak heat rate, W/cm^2	5,718	5,937	7,262	8,152	8,570
Periapsis raise ΔV, m/s	82.22	87.95	101.67	315.46	372.18
Apoapsis correction ΔV, m/s	0.04	0.18	51.43	1,840.71	2,352.62
Total propulsive ΔV, m/s	94.83	95.22	152.84	2,158.23	2,724.80

Prograde entry				
Percentage captured			98.48	
Percentage within ±50,000 km of target			95.88	

Statistics for the 98.48% cases captured					
Parameter	Minimum	0.13 percentile	Median	99.87 percentile	Maximum
Apoapsis altitude, km	144,476	183,243	382,066	3,222,790	46,519,543
Peak deceleration, Earth g	4.75	4.95	8.87	13.40	13.97
Peak heat rate, W/cm^2	1,264	1,287	1,502	1,675	1,747
Periapsis raise ΔV, m/s	0.92	13.00	97.85	179.77	212.34
Apoapsis correction ΔV, m/s	0.08	0.33	29.88	680.80	942.22
Total propulsive ΔV, m/s	93.34	94.73	127.71	843.59	1154.76

Fig. 18 Apoapsis versus periapsis altitude for reduced atmospheric uncertainty (retrograde entry). Note the improvement compared with the full range of Fminmax (Fig. 14).

Fig. 19 Apoapsis versus periapsis altitude for reduced atmospheric uncertainty (prograde entry). Of the cases, 99.9% achieved apoapsis within 50,000 km of the target.

2. Prograde Entry

Of the cases, 99.98% captured successfully and 99.9% achieved apoapsis within ±50,000 km of the target apoapsis as shown in Fig. 19. Two cases (0.04%) captured but with apoapsis altitudes of 1 million and 2.8 million km as compared with the target 400,000 km. Compared with the retrograde entry results shown in Fig. 18, the improved apoapsis targeting accuracy for the prograde entry lowered the 99.87-percentile apoapsis correction ΔV from 328 to 55 m/s. Table 9 summarizes the results for the prograde entry case with reduced atmospheric uncertainty.

The reduced atmospheric uncertainty is likely more realistic compared with the conservative full range of Fminmax [48]. In addition, the present study uses a uniform distribution for range of Fminmax considered to provide conservative estimates. For future studies, with more information available to reduce the atmospheric uncertainties, a more reasonable choice would be a normal distribution about the most likely value of Fminmax.
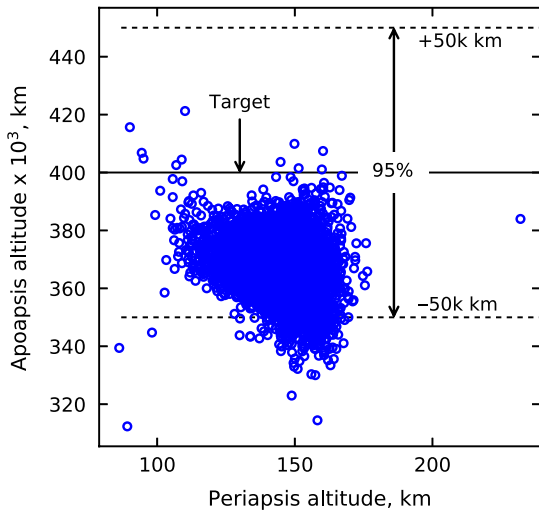
C. Very Low Atmospheric Uncertainty

To illustrate the effect of very low atmospheric uncertainty as may be possible using data from a pathfinder probe, the simulation is run with $0.6 \leq$ Fminmax ≤ 0.8, and rpscale $= 0.5$ as discussed in Sec. VII. Based on the discussion presented in Sec. VII the target EFPA is adjusted to -11.00 deg for the retrograde entry to allow for sufficient margin against escape and undershoot as indicated in Fig. 12. The target EFPA for the prograde entry is adjusted to -13.71 deg. Other simulation parameters are the same as listed in Sec. VIII.A. One hundred percent of the cases captured successfully for both retrograde and prograde entry scenarios. Figures 20 and 21 show the achieved apoapsis versus periapsis altitude for retrograde and prograde entry, respectively.

The results illustrate the effect of significant reduction of atmospheric uncertainties on apoapsis targeting accuracy. Apoapsis targeting is significantly improved compared with the simulations with the full range of Fminmax but shows only a marginal improvement compared with $-0.5 \leq$ Fminmax $\leq +0.5$. The results indicate that

Table 9   Statistics from Monte Carlo simulation with reduced atmospheric uncertainty

Retrograde entry				
Percentage captured			100	
Percentage within ±50,000 km of target			92.60	
Statistics for the 100% cases captured				
Parameter	Minimum	0.13 percentile	Median	99.87 percentile	Maximum
Apoapsis altitude, km	169,065	257,918	368,495	430,094	435,187
Peak deceleration, Earth g	4.94	5.92	7.52	11.82	12.26
Peak heat rate, W/cm^2	5,701	5,881	6,921	7,631	7,703
Periapsis raise ΔV, m/s	88.77	89.77	101.59	137.90	190.05
Apoapsis correction ΔV, m/s	0.14	1.16	53.33	328.47	754.09
Total propulsive ΔV, m/s	95.36	96.57	154.94	466.31	944.14
Prograde entry				
Percentage captured			99.98	
Percentage within ±50,000 km of target			99.90	
Statistics for the 99.98% cases captured				
Parameter	Minimum	0.13 percentile	Median	99.87 percentile	Maximum
Apoapsis altitude, km	263,169	368,826	381,941	425,621	2,778,000
Peak deceleration, Earth g	4.84	5.31	8.78	12.45	12.78
Peak heat rate, W/cm^2	1,280	1,317	1,489	1,645	1,681
Periapsis raise ΔV, m/s	14.97	90.93	97.85	101.46	136.46
Apoapsis correction ΔV, m/s	0.27	1.84	29.65	55.16	590.61
Total propulsive ΔV, m/s	95.65	97.35	127.43	155.79	605.58

Fig. 20 **Apoapsis versus periapsis altitude for very low atmospheric uncertainty (retrograde entry). Note the significant improvement compared with Figs. 14 and 18.**
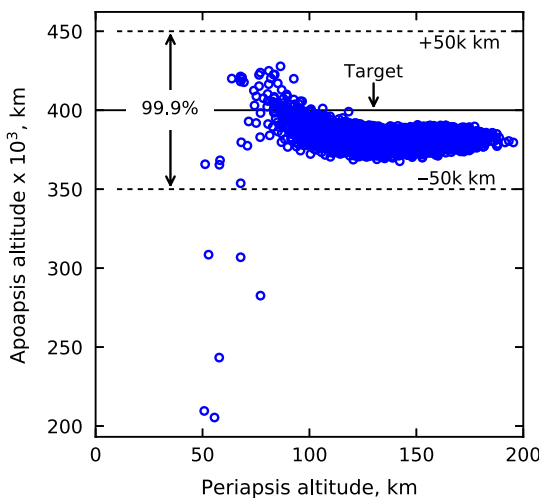
Fig. 21 **Apoapsis versus periapsis altitude for very low atmospheric uncertainty (prograde entry). The accuracy is significantly improved compared with Fig. 16, but is similar to Fig. 19.**

if $-0.5 \leq$ Fminmax $\leq +0.5$ is considered acceptable atmospheric uncertainty, a pathfinder probe is not required to provide satisfactory apoapsis targeting. However, if available, a pathfinder probe will provide additional safety margin against unknown atmospheric phenomena not accounted for in theoretical models. Table 10 summarizes the percentiles for various parameters for the very low atmospheric uncertainty scenario. For the retrograde entry, the 99.87-percentile total propulsive ΔV required is 233 m/s compared with 466 m/s for the simulations with $-0.5 \leq$ Fminmax $\leq +0.5$. In both Figs. 20 and 21, the mean apoapsis altitude falls slightly short of the target 400,000 km. This undershoot is attributed to two reasons:

1) The guidance algorithm predicts exit conditions with full lift up. Once the full lift command is initiated, the vehicle takes a few seconds to roll from its current orientation to full lift up, but the delay is not accounted for in the guidance scheme.

2) The estimated density model is not perfect and occasionally shows significant deviation below the minimum altitude at which a measurement was available. Further fine-tuning of the guidance parameters may reduce the targeting errors.

D. Sensitivity to Lift-to-Drag Ratio

The aerodynamic L/D is the most important vehicle control parameter for trajectory analysis L/D [62], and the designer must

account for the effect of variation in L/D on vehicle performance [63]. Even though the present study uses $L/D = 0.4$ as a nominal value for blunt-body aeroshells, the flight-derived L/D values for the heritage Apollo entry vehicles range from 0.280 to 0.368 [62,64]. For the purpose of the L/D sensitivity analysis, a capture probability of 98%, and 75% probability of achieving apoapsis within 50,000 km of the target are arbitrarily defined as the required criteria for mission success. A trade study is performed for $L/D = 0.35$ and 0.30 and various levels of atmospheric uncertainties to see if they offer sufficient control authority. The results are for retrograde entry.

For simulations with $-1 \leq$ Fminmax $\leq +1$, $L/D = 0.35$ and 0.30 did not meet the success criteria. To ensure capture for these cases, the target EFPA is substantially biased toward the steep end of the corridor. This results in satisfactory capture rates, but it also results in a large number of cases undershooting the target apoapsis as seen in the apoapsis altitude statistics in Tables 11 and 12. The study recommends a vehicle with L/D of at least 0.40 for such large atmospheric uncertainties if the target apoapsis of 400,000 km is desired. If the mission designer chooses to accept a wide apoapsis altitude distribution as listed in Tables 11 and 12, then $L/D = 0.35$ and 0.30 may be sufficient.

For $-0.5 \leq$ Fminmax $\leq +0.5$, $L/D = 0.35$ satisfied the success criteria, whereas $L/D = 0.30$ did not. For $L/D = 0.35$, only 83% achieved apoapsis within 50,000 km of the target compared with 93% for $L/D = 0.40$. For $L/D = 0.30$, EFPA biasing is able to once again provide satisfactory capture rates, but a significant fraction of the cases undershoot the target apoapsis. L/D of at least 0.35 is recommended for atmospheric uncertainty of $-0.5 \leq$ Fminmax $\leq +0.5$.

For $+0.6 \leq$ Fminmax $\leq +0.8$, $L/D = 0.35$ offers sufficient control authority as seen in Table 11. One hundred percent of the cases captured, and the 99.87-percentile total propulsive ΔV required is 250 m/s. For $L/D = 0.30$, EFPA biasing is required to ensure vehicle capture, but 79% of the cases achieved apoapsis within 50,000 km of the target. The study recommends L/D of at least 0.30 for $+0.6 \leq$ Fminmax $\leq +0.8$. The results of the L/D trade study are summarized in Table 13, and the simulation statistics show the effect of L/D reduction in aerocapture performance.

IX. Summary

The present study investigated the feasibility and guidance performance of using heritage low-L/D blunt-body aeroshells for aerocapture at Neptune. Previous studies addressing Neptune aerocapture have used a mid-L/D vehicle that would in turn require the design, development, and testing of a new aeroshell before use in planetary missions. The lack of a mid-L/D vehicle motivated the investigation of techniques that may allow the use of low-L/D blunt-body aeroshells that have been extensively tested and flown. The aerocapture feasibility chart is used to concisely assess the coupling between interplanetary trajectory and vehicle performance trade space during preliminary mission design. Interplanetary trajectories with high arrival V_∞ allow the vehicle L/D requirement to be lowered while providing significantly shorter time of flight to Neptune. An Earth–Jupiter–Neptune trajectory launching in 2031 with a 7.87-year flight time is selected as the reference trajectory. Approach navigation analysis using state-of-the-art techniques have shown that delivery errors can be reduced compared with previous estimates. A new guidance algorithm with onboard density estimation is shown to be able to guide the spacecraft to the desired exit conditions even in worst-case atmospheric uncertainties. The study concludes that the first hybrid aerocapture-propulsive approach does not allow the use of low-L/D aeroshells for acceptable ΔV penalty, though this conclusion holds only for the 20-day science orbit considered. Smaller science orbits of the order of 1 day or smaller may use this approach without the prohibitively large ΔV associated with this approach. The second hybrid approach also does not allow the use of heritage blunt-body aeroshells. The study finds that a pathfinder probe is not necessary for aerocapture at Neptune if the risk of apoapsis undershoot is within acceptable limits. The pathfinder probe is recommended to be used as an option to enhance the safety margins and probability of mission success, but not as an enabling option for ice giant missions. Monte Carlo simulation is used

Table 10   Statistics from Monte Carlo simulation with very low atmospheric uncertainty

Retrograde entry					
Percentage captured			100		
Percentage within ±50,000 km of target			95.08		
Statistics for the 100% cases captured					
Parameter	Minimum	0.13 percentile	Median	99.87 percentile	Maximum
Apoapsis altitude, km	312,349	333,208	367,388	404,061	421,240
Peak deceleration, Earth g	3.91	5.49	6.68	9.86	10.83
Peak heat rate, W/cm^2	5,535	5,833	6,553	7,226	7,366
Periapsis raise ΔV, m/s	90.58	93.43	100.93	100.95	117.30
Apoapsis correction ΔV, m/s	1.65	4.39	55.35	123.59	171.63
Total propulsive ΔV, m/s	94.89	98.81	156.27	232.77	288.94
Prograde entry					
Percentage captured			100		
Percentage within ±50,000 km of target			99.88		
Statistics for the 100% cases captured					
Parameter	Minimum	0.13 percentile	Median	99.87 percentile	Maximum
Apoapsis altitude, km	205,390	359,571	381,427	421,065	427,788
Peak deceleration, Earth g	6.00	6.40	8.87	11.80	13.16
Peak heat rate, W/cm^2	1,317	1,337	1,468	1,586	1,597
Periapsis raise ΔV, m/s	89.95	91.36	97.79	105.09	164.91
Apoapsis correction ΔV, m/s	0.28	0.75	30.51	70.10	543.47
Total propulsive ΔV, m/s	95.32	95.88	128.38	175.15	708.38

to test guidance performance with combined navigation, atmospheric, and aerodynamic uncertainties.

X.   Conclusions

Results indicate that the reduced navigation uncertainty and the improved guidance scheme enable a heritage blunt-body aeroshell with $L/D = 0.30$–0.40 to perform aerocapture at Neptune. The expected peak heat rate is in the range of 1600–8150 W/cm^2 and is within the capabilities of HEEET TPS material which has been tested upto 8000 W/cm^2. For a vehicle with $L/D = 0.40$ entering retrograde and even with worst-case atmospheric uncertainty, 99.98% of the cases captured successfully and 75% of the cases achieved apoapsis altitude within 50,000 km of the target. For the lower atmospheric uncertainty levels considered, the L/D of 0.3–0.4 is shown to provide satisfactory performance. Additional study is required to estimate the TPS mass fraction of blunt-body vehicles entering Neptune at planet-relative speeds of 28–33 km/s.

Table 11   Statistics from Monte Carlo simulation with $L/D = 0.35$

$-1.0 \leq$ Fminmax $\leq +1.0$; *retrograde entry*, EFPA $= -11.58$ deg *(biased to the steep side to ensure capture)*					
Percentage captured			100		
Percentage within ±50,000 km of target			44.75		
Statistics for the 100% cases captured					
Parameter	Minimum	0.13 percentile	Median	99.87 percentile	Maximum
Apoapsis altitude, km	26,799	28,526	293,630	441,328	448,812
Periapsis raise ΔV, m/s	86.67	87.96	124.00	489.27	503.09
Total propulsive ΔV, m/s	95.09	95.33	344.09	4,023	4,140
$-0.5 \leq$ Fminmax $\leq +0.5$; *retrograde entry*, EFPA $= -11.33$ deg					
Percentage captured			100		
Percentage within ±50,000 km of target			83.44		
Statistics for the 100% cases captured					
Parameter	Minimum	0.13 percentile	Median	99.87 percentile	Maximum
Apoapsis altitude, km	73,049	92,774	368,664	436,622	442,759
Periapsis raise ΔV, m/s	87.30	88.30	101.50	282.54	325.74
Total propulsive ΔV, m/s	94.63	95.31	154.53	1,840	2,260
$+0.6 \leq$ Fminmax $\leq +0.8$; *retrograde entry*, EFPA $= -10.94$ deg					
Percentage captured			100		
Percentage within ±50,000 km of target			90.38		
Statistics for the 100% cases captured					
Parameter	Minimum	0.13 percentile	Median	99.87 percentile	Maximum
Apoapsis altitude, km	287,017	326,223	364,423	407,931	430,583
Periapsis raise ΔV, m/s	88.54	92.26	101.39	111.37	125.62
Total propulsive ΔV, m/s	94.00	95.57	162.13	250.46	363.71

Table 12   Statistics from Monte Carlo simulation with $L/D = 0.30$

$-1.0 \leq$ Fminmax $\leq +1.0$; *retrograde entry*, EFPA $= -11.61$ deg *(biased to the steep side to ensure capture)*					
Percentage captured			100		
Percentage within $\pm 50{,}000$ km of target			20.00		
Statistics for the 100% cases captured					
Parameter	Minimum	0.13 percentile	Median	99.87 percentile	Maximum
Apoapsis altitude, km	5,811	8,815	93,028	441,715	446,133
Periapsis raise ΔV, m/s	86.89	87.63	280.96	670.02	760.56
Total propulsive ΔV, m/s	95.54	95.87	1,835	5,781	6,225
$-0.5 \leq$ Fminmax $\leq +0.5$; *retrograde entry*, EFPA $= -11.33$ deg *(biased to the steep side to ensure capture)*					
Percentage captured			100		
Percentage within $\pm 50{,}000$ km of target			61.50		
Statistics for the 100% cases captured					
Parameter	Minimum	0.13 percentile	Median	99.87 percentile	Maximum
Apoapsis altitude, km	54,508	55,198	361,561	426,603	430,035
Periapsis raise ΔV, m/s	89.25	89.42	103.04	367.21	370.15
Total propulsive ΔV, m/s	94.53	95.44	169.12	2,770	2,795
$+0.6 \leq$ Fminmax $\leq +0.8$; *retrograde entry*, EFPA $= -10.93$ deg *(biased to the steep side to ensure capture)*					
Percentage captured			100		
Percentage within $\pm 50{,}000$ km of target			79.44		
Statistics for the 100% cases captured					
Parameter	Minimum	0.13 percentile	Median	99.87 percentile	Maximum
Apoapsis altitude, km	77,679	124,057	363,001	408,606	419,946
Periapsis raise ΔV, m/s	90.36	92.04	101.56	230.23	309.98
Total propulsive ΔV, m/s	93.82	95.07	164.97	1,370	2,145

Table 13   Percentage captured for various L/D and atmospheric uncertainty levels

Fminmax range	Remark	L/D 0.4	0.35	0.30
-1.0 to $+1.0$	Maximum	99.9% (75%)	100%[a] (45%)	100%[a] (20%)
-0.5 to $+0.5$	Reduced	100% (93%)	100% (83%)	100%[a] (62%)
0.6 to 0.8	Very low	100% (98%)	100% (90%)	100%[a] (79%)

Values in parentheses indicate percentage of cases that achieved apoapsis within 50,000 km of the target.
[a]With EFPA biasing to the steep side to ensure capture, resulting in apoapsis undershoot. See Tables 11 and 12 for apoapsis distribution.

Appendix: Guidance Parameters

The gain parameters used in the equilibrium glide phase guidance is computed based on the procedure developed by Cerimele and Gamble [55]. The vehicle altitude dynamic response can be shown as

$$\ddot{h} + \frac{C_L S}{m} G_{\dot{h}} \dot{h} - \frac{C_L S}{m} G_{\bar{q}} (\bar{q} - \bar{q}_{\text{ref}}) = 0 \qquad (A1)$$

Equation (A1) can be approximated as a linear second-order system by assuming $\bar{q} = ah + b$, and the system response is characterized by

$$\omega_n^2 = -\frac{C_L S}{m} G_{\bar{q}} a \qquad (A2)$$

$$2\zeta \omega_n = \frac{C_L S}{m} G_{\dot{h}} \qquad (A3)$$

For a vehicle with $m/C_L S = 500$ kg/m^2 and $L/D = 0.4$ entering Neptune atmosphere retrograde with planet-relative speed $V = 33.0$ km/s, EFPA $= -11.30$ deg, and using full lift up, the dynamic pressure as a function of altitude is shown in Fig. A1. A linear approximation can be made for the pressure profile as the vehicle descends below 300 km, and the aerodynamic forces become significant. Using $\omega_n = 0.05$ rad/s and $\zeta = 1.50$, the gain parameters can be calculated as $G_{\dot{h}} = 75.0$ and $G_{\bar{q}} = 7.41$. However, adjusting $G_{\bar{q}}$ to 3.0 was found to provide better performance and hence is the value used in the study. These values provided acceptable vehicle response and were used for all simulations in the present study, including the prograde cases for consistency. For a vehicle with different $m/C_L S$, or for different entry conditions, the above procedure can be used to recalculate the gain parameters.
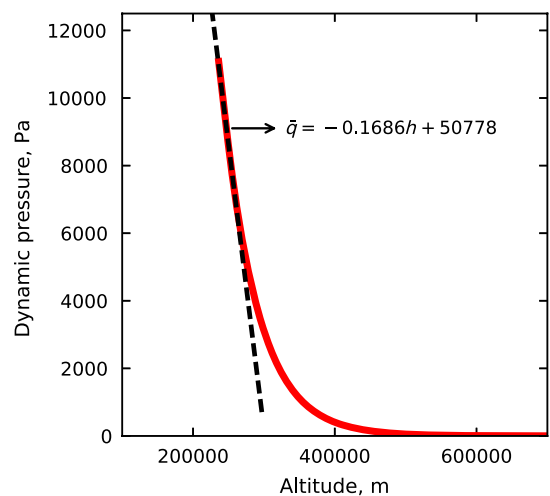
Fig. A1   Actual dynamic pressure profile (solid line) and linear approximation (dashed line) used to calculate guidance scheme gain parameters. Based on the method developed by Cerimele and Gamble [55].

Acknowledgments

References

[1] Lockwood, M. K., Edquist, K. T., Starr, B. R., Hollis, B. R., Hrinda, G. A., Bailey, R. W., Hall, J. L., Spilker, T. R., Noca, M. A., and O'Kongo, N., "Aerocapture Systems Analysis for a Neptune Mission," NASA TM-2006-214300, 2006, https://ntrs.nasa.gov/archive/nasa/casi.ntrs.nasa.gov/20060012088.pdf.

[2] Spilker, T. R., "Significant Science at Titan and Neptune from Aero-captured Missions," *Planetary and Space Science*, Vol. 53, No. 5, 2005, pp. 606–616.
https://doi.org/10.1016/j.pss.2004.12.003

[3] Allen, M. S., *NASA Space Science Vision Missions*, AIAA, Reston, VA, 2008, Chap. 3.
https://doi.org/10.2514/4.866920

[4] Spilker, T. R., Adler, M., Arora, N., Beauchamp, P. M., Cutts, J. A., Munk, M. M., Powell, R. W., Braun, R. D., and Wercinski, P. F., "Qualitative Assessment of Aerocapture and Applications to Future Missions," *Journal of Spacecraft and Rockets*, Vol. 56, No. 2, 2018, pp. 536–545.
https://doi.org/10.2514/1.A34056

[5] Carpenter, R., "Aeroasist Flight Experiment," Texas Space Grant Consortium TR ASE 396, Austin, TX, 1992, http://www.tsgc.utexas.edu/archive/PDF/AeroassistFlightExp.pdf.

[6] Wercinski, P., Henline, W., Tran, H., Milos, F., Papadopoulos, P., Chen, Y.-K., Venkatapathy, E., Tauber, M., Wercinski, P., Henline, W., and Tran, H., "Trajectory, Aerothermal Conditions, and Thermal Protection System Mass for the MARS 2001 Aerocapture Mission," *35th Aerospace Sciences Meeting and Exhibit*, AIAA Paper 1997-472, 1997.
https://doi.org/10.2514/6.1997-472

[7] Powell, R., "Numerical Roll Reversal Predictor Corrector Aerocapture and Precision Landing Guidance Algorithms for the Mars Surveyor Program 2001 Missions," *23rd Atmospheric Flight Mechanics Conference*, AIAA Paper 1998-4574, 1998.
https://doi.org/10.2514/6.1998-4574

[8] Cazaux, C., Naderi, F., Whetsel, C., Beaty, D., Gershman, B., Kornfeld, R., Mitcheltree, B., and Sackheim, B., "The NASA/CNES Mars Sample Return—A Status Report," *Acta Astronautica*, Vol. 54, No. 8, 2004, pp. 601–617.
https://doi.org/10.1016/j.actaastro.2003.07.001

[9] Keys, A., Hall, J., Oh, D., and Munk, M., "Overview of a Proposed Flight Validation of Aerocapture System Technology for Planetary Missions," *42nd AIAA/ASME/SAE/ASEE Joint Propulsion Conference & Exhibit*, AIAA Paper 2006-4518, 2006.
https://doi.org/10.2514/6.2006-4518

[10] Hall, J. L., Noca, M. A., and Bailey, R. W., "Cost-Benefit Analysis of the Aerocapture Mission Set," *Journal of Spacecraft and Rockets*, Vol. 42, No. 2, 2005, pp. 309–320.
https://doi.org/10.2514/1.4118

[11] Lockwood, M. K., Starr, B. R., Paulson, J. W., Jr., Kontinos, D. A., Chen, Y., Laub, B., Olejniczak, J., Wright, M. J., Takashima, N., and Justus, C. G., "Systems Analysis for a Venus Aerocapture Mission," NASA TM-2006-214291, 2006, https://ntrs.nasa.gov/archive/nasa/casi.ntrs.nasa.gov/20060010899.pdf.

[12] Wright, H. S., Oh, D. Y., Westhelle, C. H., Fisher, J. L., Dyke, R. E., Edquist, K. T., Brown, J. L., Justh, H. L., and Munk, M. M., "Mars Aerocapture Systems Study," NASA TM-2006-214522, 2006, https://ntrs.nasa.gov/archive/nasa/casi.ntrs.nasa.gov/20060056070.pdf.

[13] Lockwood, M. K., Queen, E. M., Way, D. W., Powell, R. W., Edquist, K., Starr, B. W., Hollis, B. R., Zoby, E. V., Hrinda, G. A., and Bailey, R. W., "Aerocapture Systems Analysis for a Titan Mission," NASA TM-2006-214273, 2006, https://ntrs.nasa.gov/archive/nasa/casi.ntrs.nasa.gov/20060007561.pdf.

[14] Lu, Y., and Saikia, S. J., "Feasibility Assessment of Aerocapture for Future Titan Orbiter Missions," *Journal of Spacecraft and Rockets*, Vol. 55, No. 5, 2018, pp. 1125–1135.
https://doi.org/10.2514/1.A34121

[15] Lemmerman, L., and Wercinski, P., "Small Neptune Orbiter Using Aerocapture," *AIP Conference Proceedings*, Vol. 387, American Inst. of Physics, Melville, NY, 1997, pp. 101–110.
https://doi.org/10.1063/1.51918

[16] Starr, B., Westhelle, C., and Masciarelli, J., "Aerocapture Performance Analysis for a Neptune-Triton Exploration Mission," *AIAA Atmospheric Flight Mechanics Conference and Exhibit*, AIAA Paper 2004-4955, 2004.
https://doi.org/10.2514/6.2004-4955

[17] Masciarelli, J., Westhelle, C., and Graves, C., "Aerocapture Guidance Performance for the Neptune Orbiter," *AIAA Atmospheric Flight Mechanics Conference and Exhibit*, AIAA Paper 2004-4954, 2004.
https://doi.org/10.2514/6.2004-4954

[18] Mazzaracchio, A., "Heat Shield Mass Minimization for an Aerocapture Mission to Neptune," *International Journal of Aerospace Innovations*, Vol. 5, Nos. 3–4, 2013, pp. 83–93.
https://doi.org/10.1260/1757-2258.5.3-4.83

[19] Saikia, S. J., Petropoulus, A. E., and Cutts, J. A., "Aerocapture Assessment at Uranus and Neptune for NASA's Ice Giant Studies," Purdue Univ. TR PU-AAC-2016-MC-0002, West Lafayette, IN, 2016.

[20] Florence, D., "Aerothermodynamic Design Feasibility of a Generic Planetary Aero-Capture/Aeromaneuver Vehicle," *16th Thermophysics Conference*, AIAA Paper 1981-1127, 1981.
https://doi.org/10.2514/6.1981-1127

[21] Wercinski, P., Munk, M., Powell, R., Hall, J., Graves, C., and Partridge, H., "Aerocapture Technology Development Needs for Outer Planet Exploration," NASA TM-2002-211386, 2002, https://ntrs.nasa.gov/archive/nasa/casi.ntrs.nasa.gov/20020077966.pdf.

[22] Noca, M., and Bailey, R., "Mission Trades for Aerocapture at Neptune," *40th AIAA/ASME/SAE/ASEE Joint Propulsion Conference and Exhibit*, AIAA Paper 2004-3843, 2004.
https://doi.org/10.2514/6.2004-3843

[23] Laub, B., and Chen, Y., "TPS Challenges for Neptune Aerocapture," *AIAA Atmospheric Flight Mechanics Conference and Exhibit*, AIAA Paper 2004-5178, 2006.
https://doi.org/10.2514/6.2004-5178

[24] Dyke, R., and Hrinda, G., "Structural Design for a Neptune Aerocapture Mission," *AIAA Atmospheric Flight Mechanics Conference and Exhibit*, AIAA Paper 2004-5179, 2004.
https://doi.org/10.2514/6.2004-5179

[25] Starr, B., Westhelle, C., and Masciarelli, J., "Aerocapture Performance Analysis for a Neptune-Triton Exploration Mission," *AIAA Atmospheric Flight Mechanics Conference and Exhibit*, AIAA Paper 2004-4955, 2004.
https://doi.org/10.2514/6.2004-4955

[26] Bailey, R., Hall, J., Spilker, T., and O'Kongo, N., "Neptune Aerocapture Mission and Spacecraft Design Overview," *40th AIAA/ASME/SAE/ASEE Joint Propulsion Conference and Exhibit*, AIAA Paper 2004-3842, 2004.
https://doi.org/10.2514/6.2004-3842

[27] Edquist, K. T., Prabhu, R. K., Hoffman, D. A., and Rea, J. R., "Configuration, Aerodynamics, and Stability Analysis for a Neptune Aerocapture Orbiter," *AIAA Atmospheric Flight Mechanics Conference and Exhibit*, AIAA Paper 2004-4953, 2004.
https://doi.org/10.2514/6.2004-4953

[28] Hollis, B. R., Wright, M. J., Olejniczak, J., Takashima, N., Sutton, K., and Prabhu, D., "Preliminary Convective-Radiative Heating Environments for a Neptune Aerocapture Mission," *AIAA Atmospheric Flight Mechanics Conference and Exhibit*, AIAA Paper 2004-5177, 2004.
https://doi.org/10.2514/6.2004-5177

[29] Hofstadter, M. D., Simon, A., Reh, K., and Elliot, J., "Ice Giants Pre-Decadal Study Final Report," NASA TR JPL D-100520, Pasadena, CA, 2017, https://www.lpi.usra.edu/icegiants/mission_study/.

[30] Moore, J., "Scientific Goals for Exploration of the Outer Solar System," Lunar and Planetary Inst. TR OPAG-Report-Draft-Aug-2019, 2019, https://www.lpi.usra.edu/opag/goals-08-28-19.pdf.

[31] Squyres, S. W., *Vision and Voyages for Planetary Science in the Decade 2013–2022*, National Academies Press, Washington, D.C., 2011, Chap. 5.

[32] Bayon, S., Falkner, P., and Pickering, A., "CDF Study Report: Ice Giants," ESA TR CDF-187(C), Noordwijk, The Netherlands, 2019, https://sci.esa.int/s/8 JgpdVA.

[33] Agrawal, P., Allen, G. A., Sklyanskiy, E. B., Hwang, H. H., Huynh, L. C., McGuire, K., Marley, M. S., Garcia, J. A., Aliaga, J. F., and Moses, R. W., "Atmospheric Entry Studies for Uranus," *2014 IEEE Aerospace Conference*, Inst. of Electrical and Electronics Engineers, New York, 2014, pp. 1–19.
https://doi.org/10.1109/AERO.2014.6836417

[34] Hughes, K. M., "Gravity-Assist Trajectories to Venus, Mars, and the Ice Giants: Mission Design with Human and Robotic Applications," Ph.D. Thesis, Purdue Univ., West Lafayette, IN, 2016.

[35] Ellerby, D., Driver, D., Gasch, M., Mahzari, M., Milos, F., Owen, N., Peterson, K., Stackpoole, M., Venkatapathy, E., Young, Z., and Gage, P. J., "Overview of Heatshield for Extreme Entry Environment Technology (HEEET) Project," *16th International Planetary Probe Workshop (IPPW)*, Boulder, CO, June 2018, https://www.colorado.edu/event/ippw2018/sites/default/files/attached-files/aeroentrytech_7_ellerby_presid594_presslides_docid1160.pdf.

[36] Milos, F. S., "Galileo Probe Heat Shield Ablation Experiment," *Journal of Spacecraft and Rockets*, Vol. 34, No. 6, 1997, pp. 705–713. https://doi.org/10.2514/2.3293

[37] Campagnola, S., Boutonnet, A., Martens, W., and Masters, A., "Mission Design for the Exploration of Neptune and Triton," *IEEE Aerospace and Electronic Systems Magazine*, Vol. 30, No. 7, 2015, pp. 6–17. https://doi.org/10.1109/MAES.2015.140119

[38] Bienstock, B., Atkinson, D., Atreya, S., Mahaffy, P., Baines, K., Wright, M., Wright, M., Stern, A., Steffes, P., Smith, D., Frampton, R., Peltz, L., Sichi, S., Masciarelli, J., Van Cleve, J., Murrow, D., and Landin, B., "NASA Vision Mission Neptune Orbiter with Probes," NASA CR NNH04CC41C, 2005.

[39] Sergeyevsky, A. B., Snyder, G. C., and Cunniff, R. A., "Interplanetary Mission Design Handbook. Volume 1, Part 2: Earth to Mars Ballistic Mission Opportunities, 1990–2005," NASA TR JPL-PUBL-82-43-VOL-1-PT-2, Pasedena, CA, 1983, https://ntrs.nasa.gov/archive/nasa/casi.ntrs.nasa.gov/19840010158.pdf.

[40] D'Amario, L., and Watkins, M., "Mars Exploration Rovers—A New Standard for Interplanetary Navigation," *55th International Astronautical Congress*, AIAA, Reston, VA, 2004. https://doi.org/10.2514/6.IAC-04-Q.3.A.04

[41] Owen, W. M., Jr., "Methods of Optical Navigation," *AAS Spaceflight Mechanics Conference*, American Astronautical Soc. Paper 11-215, 2011, https://trs.jpl.nasa.gov/handle/2014/41942.

[42] Evans, S., Taber, W., Drain, T., Smith, J., Wu, H.-C., Guevara, M., Sunseri, R., and Evans, J., "MONTE: The Next Generation of Mission Design and Navigation Software," *CEAS Space Journal*, Vol. 10, No. 1, 2018, pp. 79–86. https://doi.org/10.1007/s12567-017-0171-7

[43] Kizner, W., "A Method of Describing Miss Distances for Lunar and Interplanetary Trajectories," *Planetary and Space Science*, Vol. 7, July 1961, pp. 125–131. https://doi.org/10.1016/0032-0633(61)90293-8

[44] Longuski, J. M., Todd, R. E., and Koenig, W. W., "Survey of Nongravitational Forces and Space Environmental Torques—Applied to the Galileo," *Journal of Guidance, Control, and Dynamics*, Vol. 15, No. 3, 1992, pp. 545–553. https://doi.org/10.2514/3.20874

[45] Stone, E., and Miner, E., "The Voyager 2 Encounter with the Neptunian System," *Science*, Vol. 246, No. 4936, 1989, pp. 1417–1421. https://doi.org/10.1126/science.246.4936.1417

[46] Justus, C., Duvall, A., and Keller, V., "Atmospheric Models for Aerocapture," *40th AIAA/ASME/SAE/ASEE Joint Propulsion Conference and Exhibit*, AIAA Paper 2004-3844, 2004. https://doi.org/10.2514/6.2004-3844

[47] Duvall, A., Justus, C., and Keller, V., "Global Reference Atmospheric Model (GRAM) Series for Aeroassist Applications," *43rd AIAA Aerospace Sciences Meeting and Exhibit*, AIAA Paper 2005-1239, 2005. https://doi.org/10.2514/6.2005-1239

[48] Justh, H., "Neptune-GRAM 2004 Documentation," NASA Marshall Space Flight Center TR Neptune-GRAM 2004, Huntsville, AL, 2004.

[49] Justus, C., Duvall, A., and Johnson, D., "Engineering-Level Model Atmospheres for Titan and Neptune," *39th AIAA/ASME/SAE/ASEE Joint Propulsion Conference and Exhibit*, AIAA Paper 2003-4803, 2003. https://doi.org/10.2514/6.2003-4803

[50] Dyakonov, A., Schoenenberger, M., and Van Norman, J., "Hypersonic and Supersonic Static Aerodynamics of Mars Science Laboratory Entry Vehicle," *43rd AIAA Thermophysics Conference*, AIAA Paper 2012-2999, 2012. https://doi.org/10.2514/6.2012-2999

[51] Dutta, S., and Braun, R. D., "Statistical Entry, Descent, and Landing Performance Reconstruction of the Mars Science Laboratory," *AIAA Atmospheric Flight Mechanics Conference*, AIAA Paper 2014-0385, 2014. https://doi.org/10.2514/6.2014-0385

[52] Schoenenberger, M., Norman, J. V., Karlgaard, C., Kutty, P., and Way, D., "Assessment of the Reconstructed Aerodynamics of the Mars Science Laboratory Entry Vehicle," *Journal of Spacecraft and Rockets*, Vol. 51, No. 4, 2014, pp. 1076–1093. https://doi.org/10.2514/1.A32794

[53] Hillje, E. R., "Entry Flight Aerodynamics from Apollo Mission AS-202," NASA TN D-4185, Oct. 1967, https://ntrs.nasa.gov/archive/nasa/casi.ntrs.nasa.gov/19670027745.pdf.

[54] Way, D. W., Powell, R. W., Chen, A., Steltzner, A. D., San Martin, A. M., Burkhart, P. D., et al., "Mars Science Laboratory: Entry, Descent, and Landing System Performance," *2007 IEEE Aerospace Conference*, Inst. of Electrical and Electronics Engineers, New York, March 2007, pp. 1–19. https://doi.org/10.1109/AERO.2007.352821

[55] Cerimele, C., and Gamble, J., "A Simplified Guidance Algorithm for Lifting Aeroassist Orbital Transfer Vehicles," *23rd Aerospace Sciences Meeting*, AIAA Paper 1985-348, 1985. https://doi.org/10.2514/6.1985-348

[56] Roelke, E., Hattis, P. D., and Braun, R., "Improved Atmospheric Estimation for Aerocapture Guidance," *2019 AAS/AIAA Astrodynamics Specialist Conference*, American Astronautical Soc. Paper 19-725, 2019.

[57] Hamel, J. F., and Lafontaine, J. D., "Improvement to the Analytical Predictor-Corrector Guidance Algorithm Applied to Mars Aerocapture," *Journal of Guidance, Control, and Dynamics*, Vol. 29, No. 4, 2006, pp. 1019–1022. https://doi.org/10.2514/1.20126

[58] Perot, E., and Rousseau, S., "Importance of an On-Board Estimation of the Density Scale Geight for Various Aerocapture Guidance Algorithms," *AIAA/AAS Astrodynamics Specialist Conference and Exhibit*, AIAA Paper 2002-4734, 2002. https://doi.org/10.2514/6.2002-4734

[59] Wagner, J., Wilhite, A., Stanley, D., and Powell, R., "An Adaptive Real Time Atmospheric Prediction Algorithm for Entry Vehicles," *3rd AIAA Atmospheric Space Environments Conference*, AIAA Paper 2011-3200, 2011. https://doi.org/10.2514/6.2011-3200

[60] Skalecki, L., Cerimele, C., and Gamble, J., "Meteorological Accuracy Requirements for Aerobraking Orbital Transfer Vehicles," *22nd Aerospace Sciences Meeting*, AIAA Paper 1984-30, 1984. https://doi.org/10.2514/6.1984-30

[61] Vinh, N. X., Busemann, A., and Culp, R. D., *Hypersonic and Planetary Entry Flight Mechanics*, Univ. of Michigan Press, Ann Arbor, MI, 1980, pp. 26–28.

[62] Hillje, E. R., "Entry Aerodynamics at Lunar Return Conditions Obtained from the Flight of Apollo 4/AS-501," NASA TN D-5399, 1969, https://ntrs.nasa.gov/archive/nasa/casi.ntrs.nasa.gov/19690029435.pdf.

[63] Graves, C. A., and Harpold, J. C., "Apollo Experience Report: Mission Planning for Apollo Entry," NASA TN D-6725, 1972, https://ntrs.nasa.gov/archive/nasa/casi.ntrs.nasa.gov/19720013191.pdf.

[64] Orloff, R., and Garber, S., *Apollo by the Numbers: A Statistical Reference*, NASA History Div., Washington, D.C., 2000.

G. E. Palmer
Associate Editor